

Cosmology with voids from the Nancy Grace Roman Space Telescope

GIOVANNI VERZA ^{1,2} GIULIA DEgni ^{3,4} ALICE PISANI ^{5,6} NICO HAMAUS ⁷ ELENA MASSARA ^{8,9}
ANDREW BENSON ¹⁰ STÉPHANIE ESCOFFIER ⁵ YUN WANG ¹¹ ZHONGXU ZHAI ^{12,13,14,15} AND OLIVIER DORÉ ^{16,17}

¹Center for Computational Astrophysics, Flatiron Institute, 162 5th Avenue, 10010, New York, NY, USA

²Center for Cosmology and Particle Physics, Department of Physics, New York University, 726 Broadway, New York, NY 10003, USA

³Dipartimento di Fisica, Università di Roma Tre, Via della Vasca Navale 84, I-00146 Roma, Italy

⁴INFN - Sezione di Roma Tre, Via della Vasca Navale 84, I-00146 Roma, Italy

⁵Aix-Marseille Université, CNRS/IN2P3, CPPM, Marseille, France

⁶Department of Astrophysical Sciences, Peyton Hall, Princeton University, Princeton, NJ 08544, USA

⁷Universitäts-Sternwarte München, Fakultät für Physik, Ludwig-Maximilians Universität, Scheinerstr. 1, 81679 München, Germany

⁸Waterloo Centre for Astrophysics, University of Waterloo, 200 University Ave W, Waterloo, ON N2L 3G1, Canada

⁹Department of Physics and Astronomy, University of Waterloo, 200 University Ave W, Waterloo, ON N2L 3G1, Canada

¹⁰Carnegie Science, 813 Santa Barbara St., Pasadena, CA, USA

¹¹IPAC, California Institute of Technology, Mail Code 314-6, 1200 E. California Blvd., Pasadena, CA 91125

¹²Department of Astronomy, School of Physics and Astronomy, Shanghai Jiao Tong University, Shanghai 200240, China

¹³Shanghai Key Laboratory for Particle Physics and Cosmology, Shanghai 200240, China

¹⁴Waterloo Center for Astrophysics, University of Waterloo, Waterloo, ON N2L 3G1, Canada

¹⁵Department of Physics and Astronomy, University of Waterloo, Waterloo, ON N2L 3G1, Canada

¹⁶Jet Propulsion Laboratory, California Institute of Technology, Pasadena, CA 91109, USA

¹⁷Cahill Center for Astronomy and Astrophysics, California Institute of Technology, Pasadena, CA 91125, USA

ABSTRACT

We provide an accurate forecast of the expected constraining power from the main void statistics—the void size function and the void-galaxy cross-correlation function—to be measured by the Roman reference High Latitude Spectroscopic Survey from the Nancy Grace Roman Space Telescope. Relying on a realistic galaxy mock lightcone, covering 2000 square degrees, we find more than 8×10^4 voids and explore their constraining power in the framework of three different cosmological models: Λ CDM, w CDM, and w_0w_a CDM. This work confirms the strong complementarity of different void statistics and showcases the constraining power to be expected from Roman voids thanks to the combination of its high tracer density and large observed volume.

Keywords: Large-scale structure, cosmology, cosmic voids

1. INTRODUCTION

Cosmic voids, the under-dense regions in the galaxy distribution, provide tight constraints on cosmological parameters (Hamaus et al. 2016, 2017; Sahlén et al. 2016; Mao et al. 2017; Hawken et al. 2017; Achitouv et al. 2017; Achitouv 2019; Sahlén 2019; Hawken et al. 2020; Hamaus et al. 2020; Nadathur et al. 2020a,b; Aubert et al. 2022; Woodfinden et al. 2022, 2023; Contarini et al. 2023; Fraser et al. 2024; Contarini et al.

2024). Thanks to their wide range of sizes (from tens to hundreds of Mpc), voids allow to access information beyond the two-point correlation function over different scales (Bayer et al. 2021; Kreisch et al. 2022; Pelli-ciari et al. 2023; Beyond-2pt Collaboration et al. 2024) and promise to provide tight constraints from large scale modern surveys (e.g., Contarini et al. 2022; Hamaus et al. 2022; Radinović et al. 2023; Bonici et al. 2023). Void statistics greatly benefit of a large observed cosmological volume paired with a small tracer separation, since they allow to extract information down to the smallest scales.

The Roman reference High Latitude Spectroscopic Survey (Roman reference HLSS) from the Nancy Grace

Roman Space Telescope, expected to launch no later than May 2027, will cover in its reference design mission 2,000 square degrees with an unprecedented high tracer number density over such a volume¹, therefore providing for the first time a cosmic void sample of exceptional quality down to a few Mpc. Due to the fact that void sizes span a wide range of scales and that a high tracer number density allows a deep sampling of voids, the target population of Roman voids will be complementary to the void populations probed by other past and ongoing spectroscopic galaxy large-scale surveys (see e.g., Hamaus et al. 2016, 2020; Aubert et al. 2022; Woodfinden et al. 2022; Contarini et al. 2023; Thiele et al. 2024), effectively opening a new window for cosmic void science.

Voids have already shown their power to constrain e.g., Ω_m and the growth rate of structures f (e.g., Hamaus et al. 2020), or the sum of neutrino masses (Thiele et al. 2024) with only a few thousand voids from the BOSS sample. The Roman voids upcoming dataset will unlock further constraints, in particular it has been shown that voids can place powerful constraints on the properties of dark energy (Pisani et al. 2015a; Verza et al. 2019, 2023), and neutrinos (Massara et al. 2015; Kreisch et al. 2019; Schuster et al. 2019; Bayer et al. 2021; Kreisch et al. 2022; Verza et al. 2023). Their sensitivity to dark energy properties is expected, since voids are the first regions to be dominated by dark energy (Lavaux & Wandelt 2012; Bos et al. 2012; Pisani et al. 2015a). Voids are also particularly sensitive to the sum of neutrino masses, since the relative neutrino density in voids is higher than in other environments (Schuster et al. 2019; Bayer et al. 2024). Also, neutrinos’ free-streaming scales for relevant values of the sum of neutrino masses correspond to the range of typical void sizes (Kreisch et al. 2019).

When observing voids from large-scale surveys, we can build various statistics. The most mature void statistic is the void-galaxy cross-correlation function (VGCF), that can be used to perform the Alcock & Paczynski (AP, 1979) test and to measure redshift-space distortions around voids. This statistic currently provides the tightest constraints from voids. Secondly, in recent years the void size function (VSF), providing the number density of voids as a function of their size, has shown sensitivity to a range of cosmological parameters (Pisani

et al. 2015a; Verza et al. 2019, 2023; Contarini et al. 2022, 2023, 2024), as well as a powerful complementarity with other probes (such as clusters, see Bayer et al. 2021; Kreisch et al. 2022; Pellicciari et al. 2023). Relying on the realistic H α mock from the 2000 square degrees galaxy lightcone (Zhai et al. 2021), this paper provides a detailed forecast of constraints to be obtained from voids measured thanks to the Nancy Grace Roman Space Telescope.

The paper is organized as follows. In Section 2 we introduce the simulation and the void finder, and in Section 3 we present the VSF analysis. Section 4 describes the VGCF analysis, and we finally conclude in Section 5 summarizing our results and discussing future developments.

2. SIMULATIONS AND VOID FINDER

In this work, we consider voids measured in the 2000 square degrees galaxy lightcone (Zhai et al. 2021), in the redshift range $1 < z < 2$. The lightcone simulates the H α galaxy redshift catalog expected from the Roman reference HLSS, and is constructed from the `unit` simulation (Chuang et al. 2019), characterized by a flat Λ CDM cosmology with parameters: $[h, \Omega_b, \Omega_m, \sigma_8, n_s, A_s] = [0.6774, 0.0462, 0.3089, 0.8147, 0.9667, 2.06 \times 10^{-9}]$, as measured by Planck Collaboration et al. (2016). The lightcone has been populated with galaxies using the `GALACTICUS` (Benson 2012) semi-analytical model (SAM). The emission line luminosities are evaluated with `CLOUDY` (Ferland et al. 2013; Merson et al. 2018) using the ionizing student spectrum of each galaxy as predicted by the SAM as input.

We identified voids in the galaxy lightcone described in Zhai et al. (2021) with the `VIDE` public toolkit² (Sutter et al. 2015). `VIDE` is a parameter-free topological void finder, which identifies minima and their surrounding basins using the Voronoi tessellation followed by the watershed transform (Schaap & van de Weygaert 2000; Platen et al. 2007), based on `ZOBOV` (Neyrinck 2008). The final `VIDE` void catalog provides many void features, the most relevant for our work being i) the volume weighted barycenter, that is the void barycenter obtained weighting by the volumes of the contributing Voronoi cells; ii) the effective radius, R_{eff} , i.e. the radius of a sphere with the same volume as the void, $R_{\text{eff}} = [(3/4\pi) \sum_i V_i]^{1/3}$, where V_i is the volume of the i^{th} Voronoi cell belonging to the void.

¹ We note that, while the Roman reference HLSS covers 2000 square degrees (Spergel et al. 2015; Wang et al. 2022), the actual survey that the Nancy Grace Roman Space telescope will execute will be decided in an open community process, and may cover an even greater cosmic volume.

² <https://bitbucket.org/cosmicvoids/vid-public/wiki/Home>

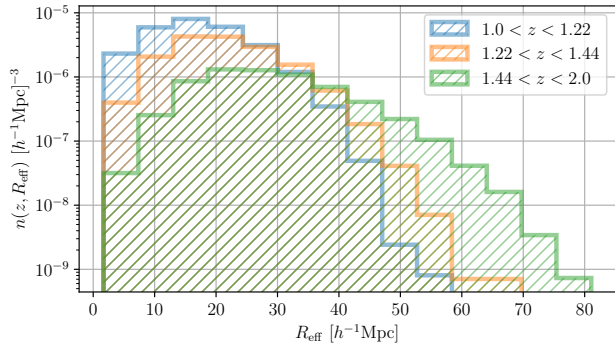


Figure 1. Histograms showing the number density of VIDE voids as a function of the void effective radius, R_{eff} . Each color corresponds to a different redshift bin, as listed in the legend.

We detect 82551 voids in the 2000 squared degrees galaxy lightcone. The redshift binning is chosen to have equipopulated bins for the VGCF analysis, that directly uses the VIDE catalog, pruning small voids (see Section 4 for details). Histograms in Figure 1 show the number density of VIDE voids as a function of the void effective radius, R_{eff} in each redshift bin considered in the analysis. The first redshift bin, $z \in [1, 1.22)$, contains 33574 voids (blue histogram), the second bin, $z \in [1.22, 1.44)$, 23114 voids (orange histogram), and the third bin, $z \in [1.44, 2]$, 25863 voids (green histogram). The higher the number density of galaxies is, the smaller the size of voids that void finders can detect over such a biased tracer distribution (Verza et al. 2023). This is visible in Figure 1 as the evolution of the radius distribution as a function of redshift.

3. THE VOID SIZE FUNCTION

3.1. Catalog preparation

The theoretical VSF describes the distribution of voids reaching a threshold value in their density contrast field. Therefore, in order to compare data with an analytical VSF model, voids are post-processed to have a fixed value in their mean density contrast in the tracer distribution where they are detected (Contarini et al. 2019; Verza et al. 2019; Contarini et al. 2022, 2023, 2024; Beyond-2pt Collaboration et al. 2024).

In this work, we explore a new methodology to post-process the void catalog. The standard methodology for post-processing watershed voids for VSF analyses (Contarini et al. 2019; Verza et al. 2019; Contarini et al. 2022, 2023, 2024) consists of growing a sphere around each void center, finding the maximum radius at which the mean density reaches the void formation threshold in

the galaxy distribution³. This methodology represents a simple and robust way to post-process VIDE voids, however it presents some arbitrariness. The first regards the choice of the void center used to grow the sphere. Usually, the standard choice is to adopt the volume-weighted barycenter provided by VIDE. This quantity is the geometrical center of the entire watershed void, and it has been shown to be ideal for measuring the VGCF (Hamaus et al. 2014, 2016, 2020, 2022). However, it is not guaranteed to be as optimal for threshold voids, which consider only the inner part of voids. The other potential issue concerns the fact that the method grows spheres, and this may introduce dependencies on the cosmology adopted to produce the catalog, a topic that recent analyses are investigating (Correa et al. 2021; Radinović et al. 2024, see Section 3.4). Moreover, overlaps among the volume of different spherical voids usually occur, leading to the introduction of criteria to select overlapping voids (usually treated as hard spheres, Contarini et al. 2019; Verza et al. 2019; Contarini et al. 2022). Finally, a spherical void finder step removes the original void shape information coming from the Voronoi tessellation and watershed algorithm, which has been shown to contain relevant cosmological information (Kreisch et al. 2022).

For this reason, we explored a new methodology that takes advantage of the entire density field estimated through the Voronoi tessellation by VIDE. For each Voronoi cell i we assign a weight equal to their volume, V_i , multiplied by the mean tracer density at the corresponding redshift z , $n_g(z)$: $w_i = V_i(z) n_g(z)$. This quantity can be interpreted as the inverse of the normalized density of the Voronoi cell, $\rho_i / \langle \rho \rangle = 1 + \delta_i$. To avoid numerical noise in the tracer density, we fit the measured tracer density with a 4th-order polynomial in z , $n_g(z) = \sum_{i=0}^4 a_i z^i$. The post-processing methodology consists of an iteration of the following steps.

- i) We select the Voronoi cell of the watershed void characterized by the highest weight $w_{i_{\text{max}}}$, i.e. the lowest density contrast, and measure the corresponding mean normalized density as $1 + \Delta_{N_v} = 1/w_{i_{\text{max}}}$. We create a set of $N_v = 1$ elements, $I_v = \{i_{\text{max}}\}$, to which, step by step, we add the cells that build up the threshold void.
- ii) We then identify the set of Voronoi cells adjacent to the selected one using the Delaunay scheme, i.e. the dual of the Voronoi tessellation (Platen et al. 2007; Neyrinck 2008), which we call A_{loop} . We grow the threshold void by adding all the Voronoi cells, moving them from

³ This methodology is conceptually similar to the spherical overdensity package of the `Subfind` algorithm used to post-process Friend-of-Friends halos (Springel et al. 2001; Dolag et al. 2009)

A_{loop} to I_v , from the highest to the lowest weight. For each added cell, we update the iteration counter by one, $N_v \rightarrow N_v + 1$, and the corresponding mean normalized density as:

$$1 + \Delta_{N_v} = \frac{\sum_{i \in I_v} n_g^{-1}(z_i)}{\sum_{i \in I_v} V_i} \simeq \frac{N_v n_g^{-1}(z_{i_{\max}})}{\sum_{i \in I_v} V_i}. \quad (1)$$

The last approximate equality follows from the fact that the redshift extension of voids is negligible with respect to the variation scale of $n_g(z)$, $\Delta z \ll 1$.

iii) If Δ_{N_v} exceeds the void formation threshold δ_v we interrupt the iteration. Otherwise, we select the Voronoi cell characterized by the highest weight w_i from A_{loop} , and we repeat step ii), avoiding to select cells already belonging to the growing threshold void.

Once all the cells belonging to the threshold void are considered, we compute the standard void quantities provided by VIDE, using the Voronoi cells information (Sutter et al. 2015). In particular in this work we consider the volume weighted barycenter, $\mathbf{X}_v = \sum_{i \in I_v} w_i \mathbf{x}_i$, where I_v is the set of Voronoi cells of the void, and the effective radius, i.e. the radius of the sphere with a volume equal to the sum of the Voronoi cells⁴,

$$R_v = \left[\frac{3}{4\pi} \sum_{i \in I_v} V_i \right]^{1/3}. \quad (2)$$

These quantities are computed considering the linearly interpolated volume fraction of the last Voronoi cell in such a way that the void formation threshold is exactly matched, i.e. f s.t. $(N_v - 1 + f) / (\sum_{j=1}^{N_v-1} w_{I_p[j]} + f w_{I_p[N_v]}) = 1 + \delta_v$, where j are the indexes of the I_v element set.

This algorithm is very similar to the watershed one (Platen et al. 2007; Neyrinck 2008), but instead of stopping at the watershed, it stops when a precise value of the mean normalized density is reached, making it specifically designed to optimize the VSF analysis. Moreover, it does not assume any symmetry in measuring the mean density contrast, making this algorithm independent on the cosmology adopted to measure distances (see Section 3.4). The algorithm is therefore more informative about the evolution of voids along cosmic history, conserving the void shape information. Additionally, the void center definition keeps the large-scale information about the low density of the environment.

3.2. Void size function model

To theoretically describe the VSF, we adopt the model presented in Verza et al. (2024). This relies on the merging of the excursion-set framework (Peacock & Heavens 1990; Bond et al. 1991) and the theory of Lagrangian density peaks (Bardeen et al. 1986), through an effective scale-dependent void formation barrier. This framework, following both the excursion-set and peak theory, describes the distribution of dark matter halos and voids in Lagrangian space, and maps the corresponding statistic in Eulerian space. We recall that the Lagrangian space is the initial density field linearly evolved up to the epoch of interest. In this context, “initial” means at redshift high enough to be fully described by linear theory, and “linearly evolved” means that the global amplitude of the density contrast field is rescaled with the linear growth factor. The Eulerian space is the fully non-linear evolution of the density field at the epoch of interest. The mapping from Lagrangian to Eulerian space is performed by considering how voids (or halos) evolve.

As in the standard excursion-set model, a void with a Lagrangian radius R is considered formed at the Lagrangian position q if R is the maximum smoothing scale at which the filtered Lagrangian density contrast field crosses the Lagrangian void formation threshold δ_v^L , without having crossed the threshold for collapse on any larger scale. The main improvements with respect to the Sheth & van de Weygaert (2004) multiplicity function can be summarized as follows: i) in the standard excursion-set framework, the position q is random, while in the model considered here, this is a minimum in the density contrast field filtered at the scale R ; ii) together with the cloud-in-cloud (or void-in-void) exclusion typical of the excursion-set, this model accounts for the peak-in-peak exclusion; iii) this model properly accounts for the smoothing of the density contrast field, which is reflected both in accounting for correlations of the density contrast field smoothed at different lengths, and considering the exact relation between the smoothing length and the Lagrangian void size. It should be noted that this last point solves the normalization problems of the Sheth & van de Weygaert (2004) multiplicity function in Eulerian space (Jennings et al. 2013). As a final remark, the Roman HLSS survey will provide a dense redshift galaxy catalog, which is reflected in the possibility of exploring voids down to small scales. Therefore, even if the Sheth & van de Weygaert (2004) model has already been used successfully to analyze BOSS data (Contarini et al. 2023, 2024), its accuracy is not sufficient for the Nancy Grace Roman Space Telescope and dense stage IV galaxy surveys: modeling the VSF over a wide range of scales requires a robust the-

⁴ We note that we use R_{eff} to indicate the effective radius of VIDE voids and R_v to indicate the effective radius of voids when post-processed with the algorithm described in this Section.

| z | α | β | γ |
|-----------|------------------------------|----------------------------|------------------------|
| 1.06–1.22 | $0.0967^{+0.0132}_{-0.0168}$ | $0.110^{+0.021}_{-0.016}$ | $1.81^{+0.25}_{-0.59}$ |
| 1.22–1.44 | $0.179^{+0.008}_{-0.007}$ | $0.0660^{+0.006}_{-0.005}$ | $2.62^{+0.70}_{-0.78}$ |
| 1.44–1.83 | $0.225^{+0.017}_{-0.004}$ | $0.0493^{+0.013}_{-0.005}$ | $1.98^{+1.05}_{-0.65}$ |

Table 1. Maximum posterior distribution values and 1D 68% CL interval for the moving barrier parameters, see Eq. (5). The first column lists the redshift bins range, the other columns list the corresponding α , β , and γ parameters, respectively.

oretical model at all scales. In fact, the Sheth & van de Weygaert (2004) and Jennings et al. (2013) models cannot reproduce the VSF measured in the 2000 square degrees galaxy lightcone (Zhai et al. 2021) adopted here, while the Verza et al. (2024) model does.

The main quantity in modeling the size distribution of halos and voids is the formation threshold. Halos are collapsed objects, so the Lagrangian threshold for halo formation is the Lagrangian density contrast corresponding to a full collapse in Eulerian space (Bond et al. 1991; Sheth et al. 2001; Lee 2010; Pace et al. 2010). However, voids do not undergo an analogous formation event and continue to expand forever (in the single-stream regime). Since voids do not undergo shell-crossing on the scales relevant to Roman (see e.g., Biswas et al. 2010; Pisani et al. 2015a), this ensures that in principle evolved voids can always be mapped in Lagrangian space and *vice versa*, considering a simple analytical map for the threshold, radius, and position (Verza et al. 2024). It follows that the Lagrangian void formation threshold can be any negative value that can be chosen according to the given survey’s features (Pisani et al. 2015a; Verza et al. 2019; Contarini et al. 2022; Verza et al. 2024), as long as the theoretical model is coherently computed.

In particular, we adopt the multiplicity function of Eq. (15) in Verza et al. (2024):

$$f(S) = \frac{e^{-B_S^2/2S}}{\sqrt{2\pi S}} \left[\sqrt{\frac{\Gamma_{\delta\delta}}{2\pi S}} \exp \left[-\frac{S}{2\Gamma_{\delta\delta}} \left(\frac{B_S}{2S} - B'_S \right)^2 \right] + \frac{1}{2} \left(\frac{B_S}{2S} - B'_S \right) \left\{ \operatorname{erf} \left[\sqrt{\frac{S}{2\Gamma_{\delta\delta}}} \left(\frac{B_S}{2S} - B'_S \right) \right] + 1 \right\} \right], \quad (3)$$

where

$$S = \sigma^2(R) = \langle \delta_S^2 \rangle = \int \frac{dk k^2}{2\pi^2} P(k) |W(kR)|^2. \quad (4)$$

with δ_S the linear density contrast field filtered at the scale $S = S(R)$, $P(k)$ the linear power spectrum, $W(kR)$

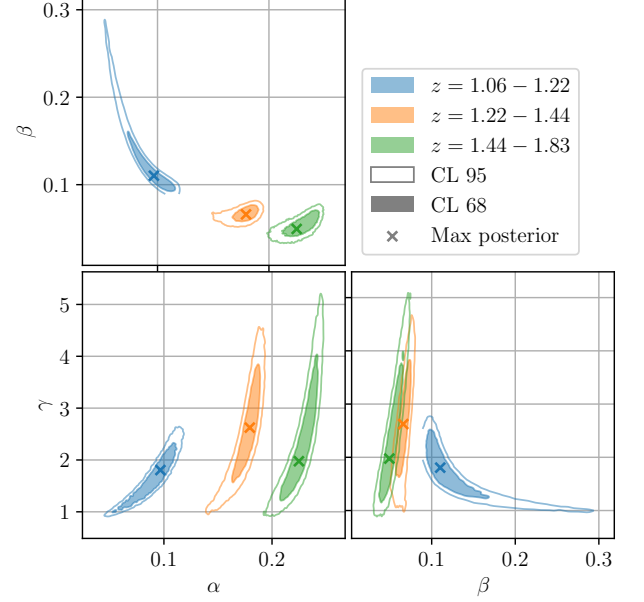


Figure 2. 2D projected posterior distributions for the moving barrier parameters, Eq. (5), for each redshift bin, as labelled in the legend. The shaded area shows the 68%CL, while the outer contours corresponds to 95%CL. The crosses show the maximum of the posterior distributions.

the top-hat filter function in Fourier space, $\Gamma_{\delta\delta} = SD_S - 1/4$, and $D_S = \langle (d\delta_S/dS)^2 \rangle$. The moving barrier $B_S = B(S, \delta_v)$, is a function of the physical void formation barrier δ_v , while $B'_S = dB(S)/dS$.

3.3. Methodology

The theoretical VSF model describes the number density of voids in the matter distribution, while in survey analyses we have access to the density contrast field of the galaxy distribution in redshift-space, that is with biased tracers. Voids are detected in this field, and therefore we have to take into account all the observational effects impacting the VSF. Some of these effects can be accounted for analytically. For example, galaxy bias in voids can be theoretically modeled, recovering the corresponding matter density contrast (Verza et al. 2022). While the apparent enlargement of voids due to redshift-space distortions can be modeled, this neglects non-linear effects (Correa et al. 2021). In fact it has been shown that even void detection can be affected (Pisani et al. 2015b; Correa et al. 2022; Massara et al. 2022; Radinović et al. 2024), and the impact on constraints is a topic currently under investigation. Various other observational effects impact the mapping from the measured VSF in the observed galaxy distribution and the corresponding one in the matter distribution. For this reason, in this work we chose to model the ef-

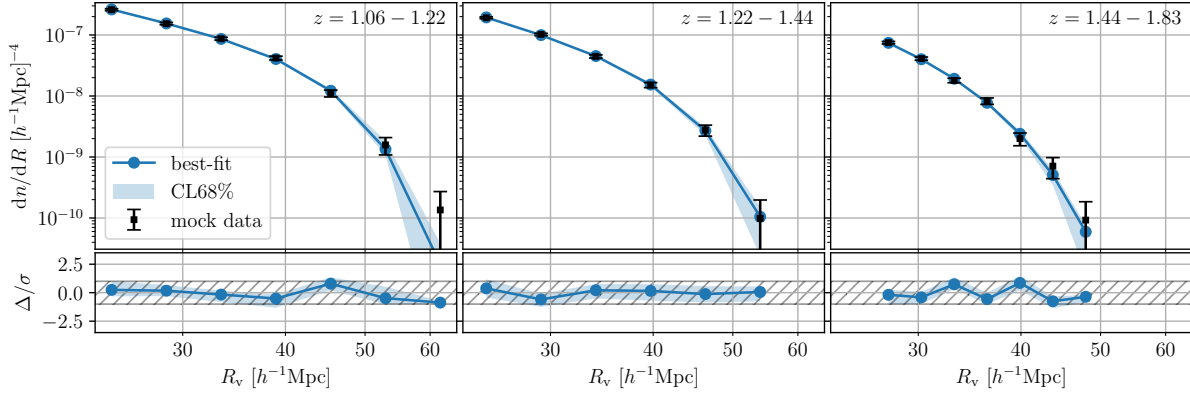


Figure 3. From left to right: VSF from the Roman reference HLSS-like mock (Zhai et al. 2021), in each of the three redshift bins considered. Upper panels: black dots with error bars show the measured VSF from the post-processed void catalog as described in Section 3.1 with $\delta_{v,g} = -0.7$, the error bars are Poissonian; blue solid lines show the best-fit moving barrier calibrated as described in Section 3.3; blue shaded areas show 68% CL. Lower panel: blue solid lines show the relatives of the best VSF theoretical model with respect to measurements in σ units; blue shaded areas show the 68% CL; gray hatched areas show the $\pm 1\sigma$ interval.

fective model barrier for void formation to account for various important observational effects, such as: galaxy bias, linear and non-linear redshift-space distortion effects, non-trivial evolution from Lagrangian to Eulerian space⁵, selection effects, etc. We use the following ansatz for the moving barrier $B_S = B(S)$,

$$B(S) = \alpha [1 + (\beta/S)^\gamma]. \quad (5)$$

The free parameters of our VSF model, namely α , β , and γ in the above equation, are functions of redshift, as they depend on the linear growth factor and on the observed tracer population. Figure 2 shows the Markov chain Monte Carlo (MCMC) best-fit of these parameters (crosses), with the 68% and 95% confidence level (CL) represented by the shaded areas and contours, respectively. Each color corresponds to a different redshift bin, as described in the legend. Table 1 lists the corresponding best-fit values and 1D 68% CL intervals. A clear redshift dependence of α and β is visible, as expected, while γ can be considered constant at the precision level allowed by simulated data. We note that, according to Eq. (5), α drives the overall height of the barrier, while β determines the scale at which the exponential cut of the VSF occurs.

It follows that, given the tracer evolution and the various observational effects we considered, the redshift dependence of these parameters is expected. Such expected redshift evolution is confirmed by the posterior distributions of the parameters used in this analysis in

each redshift bin, shown in Figure 2. While in this work we characterize these parameters independently in each redshift bin considered (which in some way accounts for a redshift dependence), this does not correspond to having a model of the redshift evolution for these parameters. Developing such a model would require for example a unique relationship depending on redshift for each parameter, and would effectively reduce the number of nuisance parameters for VSF analyses. This is, however, beyond the scope of this paper, and will be explored in a future work. Alongside the redshift evolution, the effective barrier parameterization may be affected by dependencies on cosmology and tracer population. The strongest impact is expected to come from the tracer population via their bias. This would impact the global amplitude of the barrier but not the shape. A similar cosmological dependence is expected from those parameters that modify the amplitude of the linear matter power spectrum, without impacting its shape, as, e.g., σ_8 or a dynamical dark energy component. Finally, a minor dependence on the linear matter power spectrum shape is expected, which can introduce a cosmology dependence for those parameters that impact the power spectrum shape, such as Ω_m . This is due to minor changes in the shape of the correlation between the random walk steps at different scales, from which the multiplicity function is generated. This effect is, however, expected to be sub-dominant (Verza et al. 2024). As mentioned above, exploring the redshift dependence for tracers and cosmology is beyond the scope of this work: we plan to fully characterize these dependencies in future works, by using lightcone mock realizations.

⁵ We note that in this approach, the mapping from Lagrangian to Eulerian voids is implicitly accounted for in the moving barrier modeling.

Figure 3 shows the VSF in each of the three redshift bins considered. In the upper panels, black dots with error bars show the measured VSF from the post-processed void catalog as described in Section 3.1 with $\delta_{v,g} = -0.7$, the error bars are Poissonian. Blue solid lines show the best-fit moving barrier calibrated as described in Section 3.3, while blue shaded areas show 68% confidence level (CL). In the lower panel, blue solid lines show the relatives of the best VSF theoretical model with respect to measurements in σ units, blue shaded areas show the 68% CL, and gray hatched areas show the $\pm 1\sigma$ interval.

3.4. Analysis and results

To study the constraining power of the VSF in the Roman reference HLSS, we perform a Bayesian analysis using a MCMC to sample the posterior distribution

$$\mathcal{P}(\Theta|\mathcal{D}) \propto \mathcal{L}(\mathcal{D}|\Theta) p(\Theta), \quad (6)$$

where $\mathcal{L}(\mathcal{D}|\Theta)$ is the likelihood, \mathcal{D} is the data vector, i.e. the measured VSF in the three redshift bins, Θ is the array of the cosmological parameters explored plus any extra model parameters, and $p(\Theta)$ is the prior distribution of the parameters. We consider a Gaussian likelihood using the theoretical VSF with the calibration of the effective barrier parameters, presented in Section 3.2 and 3.3,

$$\begin{aligned} \log[\mathcal{L}(\mathcal{D}|\Theta)] = & -\frac{1}{2} \sum_{ij} (n_i^{\mathcal{D}} - n_i^T) \Sigma_{ij}^{-1} (n_j^{\mathcal{D}} - n_j^T) \\ & - \frac{N_{\mathcal{D}}}{2} \log(2\pi) - \frac{1}{2} \log(\det \Sigma). \end{aligned} \quad (7)$$

The indexes $i = i(r, i_z)$ and $j = j(r, j_z)$ run over all the radius bins, i_r , of the VSF and all the redshift bins considered, i_z , i.e. i and j run from 1 to $N_{\mathcal{D}}$, which is the length of the data vector considered. The $n_i^{\mathcal{D}}$ quantity refers to the number density of voids with radius in the radius bin i_r and redshift bin i_z , n_i^T refers to the corresponding theoretical quantity, i.e. the integration of the theoretical VSF over the radius bin. Previous studies on mock catalogs showed that off-diagonal terms of the covariance matrix Σ_{ij} of the measured VSF are negligible (Bayer et al. 2021; Kreisch et al. 2022; Pelliciani et al. 2023; Contarini et al. 2023; Thiele et al. 2024), therefore we consider a diagonal covariance, where the elements correspond to the Poissonian uncertainty provided by the number of voids in a given radius and redshift bin: $\Sigma_{ij} = \sigma_i^2 \delta_{ij}^K$ where δ_{ij}^K is the Kronecker delta, $\sigma_i = \sqrt{N_i}/V_{i_z}$, N_i is the number of voids in the redshift bin i_z with radius in the radius bin i_r , and V_{i_z} is the volume of the redshift bin i_z . We note that we use here

a Gaussian likelihood instead of a Poissonian one, since in previous works (Contarini et al. 2022; Beyond-2pt Collaboration et al. 2024) we did not find any relevant difference in the posterior distribution obtained with a Gaussian or a Poissonian prior, respectively.

It is important to note that to obtain the measured VSF we assumed a cosmological model, Λ CDM, with a fixed set of cosmological parameters, which we call “fiducial cosmology”. This is because we converted the observed redshift of galaxies to comoving distances, and we ran the void finder and post-processed voids using these coordinates. At each step of the MCMC, we compute the posterior probability of an assumed “true cosmology”, likely different from the “fiducial” one. It follows that not only the theoretical model, but also the inferred number density $n_i^{\mathcal{D}}$ and the corresponding covariance Σ_{ij} change, due to the introduction of geometrical distortions: the Alcock & Paczynski (AP, 1979) and volume effects (Contarini et al. 2022; Verza et al. 2023).

The AP effect impacts the estimated void sizes and introduces an anisotropy between the orthogonal and the parallel directions with respect to the line-of-sight (LOS). Let us consider two points characterized by a mean redshift z , a difference in redshift $\Delta z \ll 1$ and an angular separation $\Delta\theta \ll 1$ rad. Their distance, decomposed in the radial and orthogonal components with respect to the LOS, is (Eisenstein et al. 2005; Xu et al. 2013):

$$\begin{aligned} r_{\parallel}^{\text{true}} &= \frac{H^{\text{fid}}(z)}{H^{\text{true}}(z)} r_{\parallel}^{\text{fid}} = q_{\parallel} r_{\parallel}^{\text{fid}}, \\ r_{\perp}^{\text{true}} &= \frac{D_A^{\text{true}}(z)}{D_A^{\text{fid}}(z)} r_{\perp}^{\text{fid}} = q_{\perp} r_{\perp}^{\text{fid}}, \end{aligned} \quad (8)$$

where $H(z)$ is the Hubble parameter and $D_A(z)$ the comoving (angular-diameter) distance. The superscripts indicate whether the corresponding quantities are computed considering the fiducial or assumed true cosmology in each MCMC step, respectively. We note that the volume of a Voronoi cell is modified exactly as $V_{\text{cell}}^{\text{true}} = q_{\parallel} q_{\perp}^2 V_{\text{cell}}^{\text{fid}}$. Therefore, by construction, following Eq. (2), the void radius transforms as $R_v^{\text{true}} = q_{\parallel}^{1/3} q_{\perp}^{2/3} R_v^{\text{fid}}$. This result is already known for voids (Hamaus et al. 2020; Correa et al. 2021; Contarini et al. 2022), for which, however, this relation is an approximation and subject to the cosmology dependence on the void finder or post-processing procedure (Correa et al. 2021; Radinović et al. 2024). In our case, relying on the Voronoi tessellation, the relation is exact in the limit in which Eqs. (8) are satisfied (Verza et al. 2023).

The volume effect changes the number density $n_i^{\mathcal{D}}$ and the associated uncertainty σ_i due to the change in the

inferred redshift bin volume,

$$V_{i_z} = \frac{\Omega_{[\text{rad}]}}{3} [D_A^3(z_{\text{out}}) - D_A^3(z_{\text{in}})] \quad (9)$$

where $\Omega_{[\text{rad}]}$ is the sky area in steradian, $D_A(z)$ is the comoving distance corresponding to an object at redshift z , while z_{in} and z_{out} are the inner and outer redshift limits of the redshift bin i_z . It follows that

$$\sigma_i^{\text{true}} = \sigma_i^{\text{fid}} \frac{D_{A,\text{fid}}^3(z_{\text{out}}) - D_{A,\text{fid}}^3(z_{\text{in}})}{D_{A,\text{true}}^3(z_{\text{out}}) - D_{A,\text{true}}^3(z_{\text{in}})}, \quad (10)$$

$$n_i^{\text{true}} = n_i^{\text{fid}} \frac{D_{A,\text{fid}}^3(z_{\text{out}}) - D_{A,\text{fid}}^3(z_{\text{in}})}{D_{A,\text{true}}^3(z_{\text{out}}) - D_{A,\text{true}}^3(z_{\text{in}})}. \quad (11)$$

The above relations assume that voids are conserved, i.e. their detection and identification do not depend on the cosmology assumed in running the void finder and in post-processing the void catalog. This condition is only approximate for spherical threshold voids (Correa et al. 2021; Radinović et al. 2024), while it is exactly satisfied by both the void finder and the post-process procedure presented in this work (see Section 3.1). This is because, under a smooth change of the tracer distance from the observer, the Voronoi tessellation would provide a different cell volume, but the topological structure does not change. In particular, the identification of the Voronoi cells corresponding to the minima in the density field does not change, as well as the identification of the Voronoi cells building up the void. In other words, the redshift and angular coordinates of the minima and void barycenter are not impacted by the assumed cosmology (Verza et al. 2023). Moreover, the threshold value is not affected by geometrical distortions, due to cancellations of the AP terms. We note that $n_g^{\text{true}}(z) = q_{\parallel}^{-1} q_{\perp}^{-2} n_g^{\text{fid}}(z)$, while $V_i^{\text{true}} = q_{\parallel} q_{\perp}^2 V_i^{\text{fid}}$. In the limit in which the AP correction is valid, $\sum_{i \in I_v} V_i^{\text{true}} = q_{\parallel} q_{\perp}^2 \sum_{i \in I_v} V_i^{\text{fid}}$, where q_{\parallel} and q_{\perp}^2 are evaluated at the redshift of the void center. From Eq. (1) it follows $\delta_v^{\text{fid}} = \delta_v^{\text{true}}$. Therefore, both the relative minima and the cells belonging to threshold voids are conserved, i.e. the void catalog is cosmology independent. We note that even this last relationship is exact for our void catalog, while it is approximate for spherical voids.

In this work, we explore three different cosmological models. The first is the flat Λ CDM model, where the cosmological parameters explored are $\Theta_{\Lambda\text{CDM}} = \{\Omega_m, \sigma_8, h\}$, while n_s is kept fixed to the value used in the simulation, see Section 2. We note that σ_8 , the normalization of the linear power spectrum at $z = 0$, has a one to one mapping with A_s , the amplitude of scalar fluctuations after inflation. In the MCMC, we explore A_s and obtain σ_8 as a derived parameter. We use

wide flat priors for all parameters, $\Omega_m \in (0.15, 0.65)$, $A_s \in (10^{-10}, 5 \times 10^{-9})$, $h \in (0.3, 2)$. The second model is the w CDM model, an extension of the Λ CDM model with a dark energy component characterized by a constant equation of state, w . The parameters explored are $\Theta_{w\text{CDM}} = \Theta_{\Lambda\text{CDM}} \cup \{w\}$. The prior distributions for the parameters in common with Λ CDM are the same as the ones adopted for Λ CDM. For w we consider a flat prior with the range $w \in (-3, 0)$. The third and last model we consider is a $w_0 w_a$ CDM model, i.e. we consider a dynamical dark energy component, characterized by the Chevallier–Polarski–Linder (CPL) equation of state (Chevallier & Polarski 2001; Linder 2003), which is the Taylor expansion of any possible equation of state truncated at the linear order,

$$w(a) = w_0 + (1 - a) w_a \Rightarrow w(z) = w_0 + \frac{z}{1 + z} w_a. \quad (12)$$

The parameters explored are $\Theta_{w_0 w_a \text{CDM}} = \Theta_{\Lambda\text{CDM}} \cup \{w_0, w_a\}$. The priors for $\Theta_{\Lambda\text{CDM}}$ parameters are as in the Λ CDM case. We use flat priors for both w_0 and w_a , with $w_0 \in (-3, 0)$, $w_a \in (-8, 5)$.

For each cosmological model, we perform two analyses, an optimistic one, in which the moving barrier parameters of Section 3.3 are considered fixed to the best fit value, and a pessimistic one, in which the effective barrier parameters are considered as nuisance parameters, using as prior for α , β , and γ of Eq. (5) of each redshift bin the posterior of the calibration described in Section 3.3, resulting in a total of 9 nuisance parameters. This choice is due to the fact that we want to explore the constraining power coming from a VSF analysis performed on Roman-like data. The optimistic scenario represents the case in which the theoretical model is fully understood and is able to provide a robust prediction; while the pessimistic case corresponds to the case in which the dependence of the moving barrier on the tracer distribution is unknown. An intermediate step among these two cases would consist of modeling the redshift dependence of the effective barrier parameters. This would considerably decrease the number of nuisance parameters; its implementation is however beyond the scope of this work. The MCMC analyses are performed using the `emcee`⁶ (Foreman-Mackey et al. 2019) Python package, considering 48 walkers. Each chain is post-processed by removing the first 2000 steps. Moreover, to ensure that the different steps are not correlated, we consider 1 chain step every 15 computed, resulting in a final chain length of around 2×10^7 , for each of the models considered.

⁶ <https://github.com/dfm/emcee>

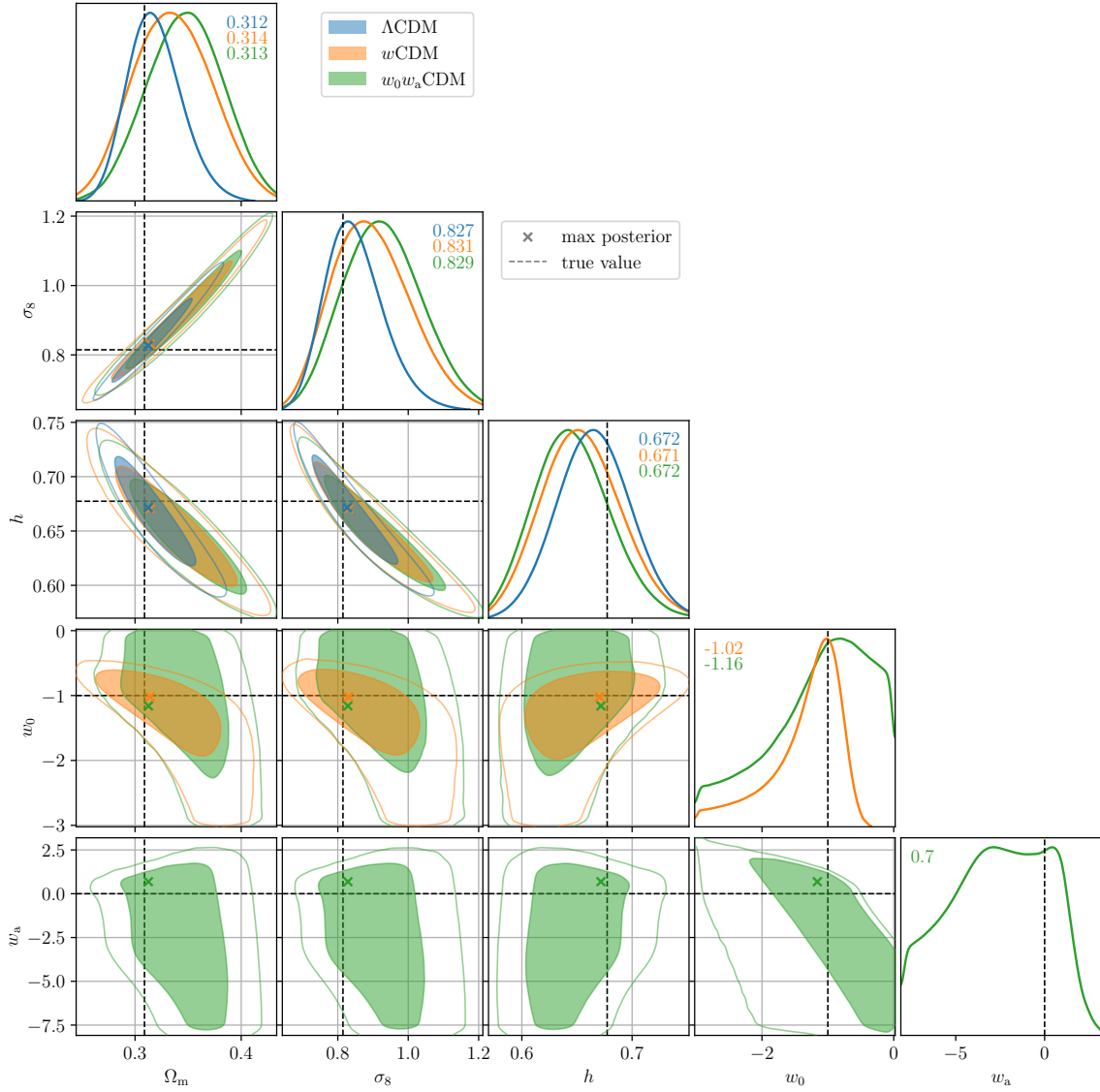


Figure 4. VSF: posterior distributions of the cosmological parameters explored in the optimistic scenario, for the three cosmological models explored: Λ CDM (blue), w CDM (orange), w_0w_a CDM (green). The filled internal region shows the 68% CL, the outer line shows the 95% CL. Black dashed lines show the true values, crosses correspond to the maximum of the posterior distribution, the numbers in the panels along the diagonal list the parameter values corresponding to the maximum of the likelihood.

Figures 4 and 5 show the 2D projected posterior distributions of the explored cosmological models, Λ CDM (blue), w CDM (orange), and w_0w_a CDM (green). Shaded areas show the 68% CL, the outer lines show the 95% CL, crosses correspond to the maximum of the posterior distribution, and dashed gray lines to the true values of the parameters. Table 2 lists the best-fit values and 1D 68% CL of each cosmological parameter in both the optimistic and pessimistic cases for each cosmological model considered. It can be noted that in the pessimistic case the 68% CL of each cosmological parameter results slightly enlarged due to the number of

nuisance parameters. It is important to recall that in a more realistic case, when the effective barrier parameters will be modeled as a function of redshift, the number of nuisance parameters will decrease with respect to the one explored here.

To conclude this section, we want to stress that this analysis considers the void size function alone. A great advantage of the VSF and other cosmic void statistics comes from their power when combined with other probes (Pisani et al. 2015a; Bayer et al. 2021; Kreisch et al. 2022; Pelliciani et al. 2023; Kreisch et al. 2022; Contarini et al. 2022). Indeed it is possible to greatly

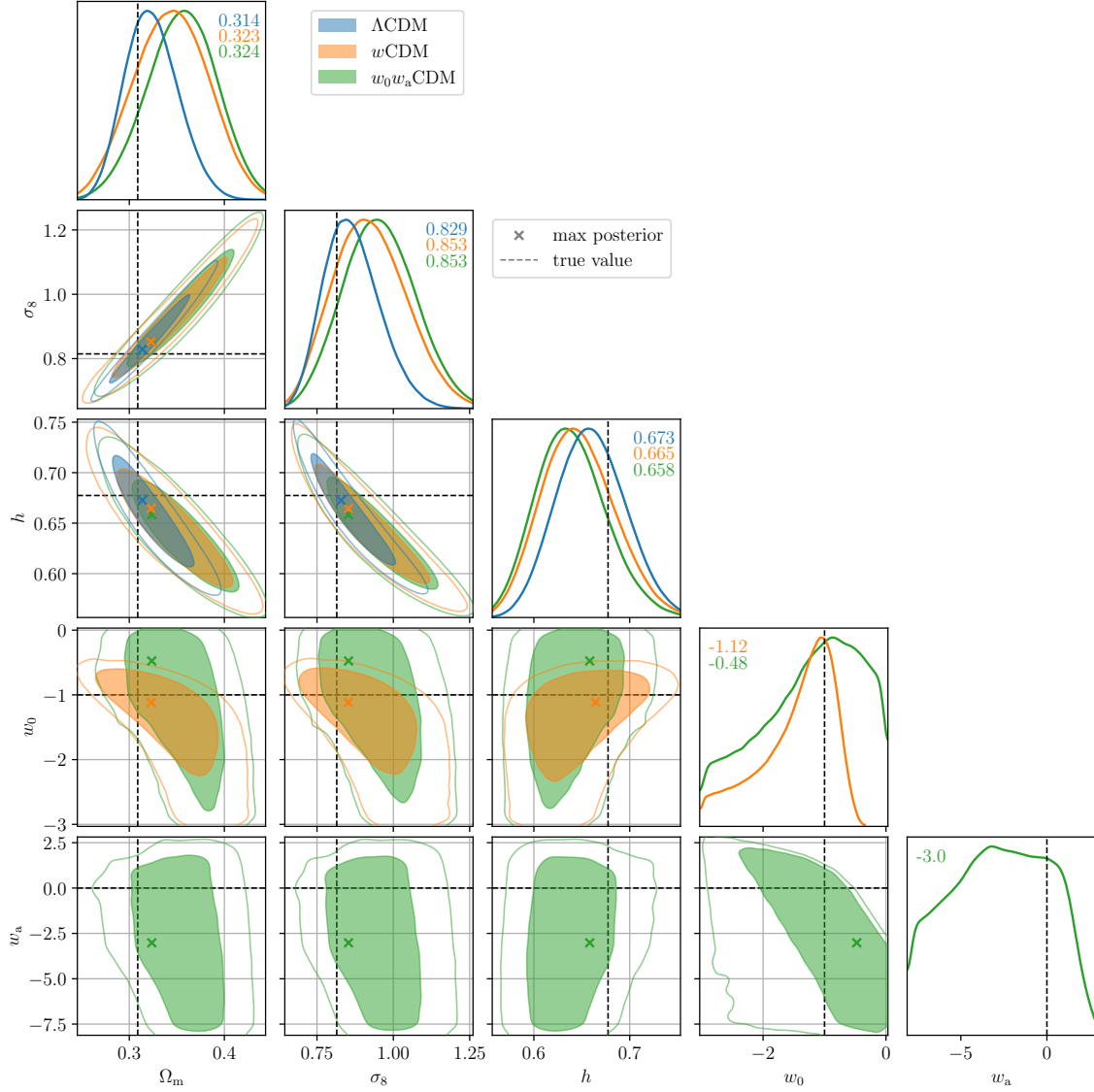


Figure 5. VSF: posterior distributions of the cosmological parameters explored in the pessimistic scenario, for the three explored cosmological models. The plot is organized as Figure 4.

tighten the constraints by combining void statistics among themselves (see e.g., Kreisch et al. 2022; Contarini et al. 2022, and discussion in Section 5), and with galaxy statistics such as cluster counts and galaxy two-point statistics (Bayer et al. 2021; Pellicciari et al. 2023; Contarini et al. 2022). The additional power is due to various reasons. Firstly, cosmic voids probe different scales with respect to clusters and galaxies (Pellicciari et al. 2023; Contarini et al. 2023). Secondly, since voids have an extended size, the AP effect on voids acts in a different way compared to how it acts on galaxy statistics. Finally, galaxies and voids probe different environments. Interestingly, the underdense environment of voids is representative of less evolved and pristine regions in the Universe (Lavaux & Wandelt 2012; Bos et al.

2012; Cautun et al. 2014; Pisani et al. 2015a; Verza et al. 2022). Also, due to their underdense nature, voids are an environment where the dark energy-dark matter density ratio is higher than in the mean universe (Cautun et al. 2014; Pisani et al. 2015a; Verza et al. 2019).

Along with the VSF, the other void statistic we consider is the VGCF, that we discuss in the following section.

4. THE VOID-GALAXY CROSS-CORRELATION FUNCTION

4.1. Theory

The void-galaxy cross-correlation function (VGCF), $\xi(r)$, quantifies the excess probability of finding a galaxy at a comoving distance r from the center of a void, com-

| Model | | Ω_m | σ_8 | h | w_0 | w_a |
|---------------|-------|------------------------------|------------------------------|------------------------------|----------------------------|-------------------------|
| True | | 0.3089 | 0.8147 | 0.6774 | -1 | 0 |
| Λ CDM | opt. | $0.3125^{+0.0283}_{-0.0216}$ | $0.8268^{+0.0880}_{-0.0714}$ | $0.6715^{+0.0263}_{-0.0395}$ | -1 | 0 |
| | pess. | $0.3138^{+0.0352}_{-0.0203}$ | $0.8288^{+0.1126}_{-0.0675}$ | $0.6726^{+0.0214}_{-0.0505}$ | -1 | 0 |
| w CDM | opt. | $0.3142^{+0.0571}_{-0.0175}$ | $0.8311^{+0.1610}_{-0.0589}$ | $0.6705^{+0.0169}_{-0.0544}$ | $-1.022^{+0.318}_{-0.542}$ | 0 |
| | pess. | $0.3230^{+0.0614}_{-0.0174}$ | $0.8527^{+0.1820}_{-0.0587}$ | $0.6645^{+0.0164}_{-0.0594}$ | $-1.117^{+0.425}_{-0.613}$ | 0 |
| $w_0 w_a$ CDM | opt. | $0.3126^{+0.0703}_{-0.0008}$ | $0.8288^{+0.1998}_{-0.0218}$ | $0.6717^{+0.0052}_{-0.0627}$ | $-1.160^{+1.160}_{-0.225}$ | $0.69^{+0.47}_{-5.28}$ |
| | pess. | $0.3237^{+0.0696}_{-0.0029}$ | $0.8533^{+0.2134}_{-0.0210}$ | $0.6583^{+0.0121}_{-0.0593}$ | $-0.476^{+0.476}_{-1.091}$ | $-3.02^{+4.20}_{-1.92}$ |

Table 2. VSF: maximum posterior distribution values and 1D 68% CL interval for the cosmological parameters explored, for each considered cosmological model (we show both the optimistic and pessimistic scenarios).

pared to what would be expected in a random, uncorrelated galaxy distribution. In essence, $\xi(r)$ measures how much more (or less) likely it is to find galaxies near void centers relative to a uniform galaxy distribution across the Universe, making it a valuable statistical tool for studying average void shapes. While individual voids exhibit a variety of shapes and sizes, by stacking voids and analyzing the resulting average void shape, we expect—based on the cosmological principle of homogeneity and isotropy—that the average void is statistically spherical in real space. Observed voids show distortions, arising when converting the measured quantities, i.e., redshifts and angular coordinates, into distances. Hence the observed stacked void profile deviates from spherical symmetry. This symmetry is disrupted by geometrical distortions, such as AP distortions, which arise from the use of an incorrect cosmological model when converting from redshifts and sky coordinates to distances, and redshift space distortions (RSD), which are caused by Doppler shifts due to the peculiar velocities of galaxies along the line of sight. Through the modelling of such distortions, the VGCF is widely used in void cosmology as a tool for constraining cosmological parameters (e.g., Hamaus et al. 2017, 2020; Nadathur et al. 2020b; Radinović et al. 2023; Correa et al. 2022; Fraser et al. 2024). Specifically, geometric distortions enable the so-called AP test. This test relies on the principle that stacked voids will only appear spherically symmetric if the fiducial cosmological model used to convert redshifts into distances is correct (Ryden 1995; Lavaux & Wandelt 2012). To perform a successful AP test, it is essential to account for the presence of RSD, which requires careful modeling of peculiar velocities. These velocities can be modeled analytically by adopting a linear approximation (Peebles 1980; Kaiser 1987),

as described below, or can be modeled numerically by employing reconstruction algorithms (see Degni et al. in prep). For this scope, cosmic voids provide an optimal environment. In fact other cosmic web structures, such as galaxy clusters, filaments, and walls, underwent shell-crossing in early stages of their evolution. This breaks both the validity of linear theory, and the Lagrangian fluid trajectories on which the above mentioned numerical methods rely. On the other hand cosmic voids are in the mildly non-linear regime, evolving in the single stream regime, reaching only mild or no shell-crossing in their inner regions (Shandarin 2011; Abel et al. 2012; Sutter et al. 2014a; Hahn et al. 2015; Schuster et al. 2023, 2024).

The relative peculiar velocity field \mathbf{u} with respect to the void center is the source of RSDs. Since the integrated density profile of a void $\Delta(r)$ obeys spherical symmetry,

$$\Delta(r) = \frac{3}{r^3} \int_0^r \delta(r') r'^2 dr', \quad (13)$$

the relative velocity field \mathbf{u} is robustly described by linear theory (Peebles 1980)

$$\mathbf{u} = -\frac{f(z)}{3} \frac{H(z)}{1+z} \Delta(r) \mathbf{r}, \quad (14)$$

where \mathbf{r} is the comoving distance from the void center (in real space) and δ the matter density contrast for the spherically symmetric stacked void. Work with high-resolution N-body simulations shows that this spherical and linear approximation can accurately describe the velocity profile of stacked voids from large to very small scales, of the order of $\sim 1h^{-1}\text{Mpc}$ (Hamaus et al. 2014; Schuster et al. 2023, 2024). This is likely due to the single-stream regime characterizing voids' evolution. In fact, according to the Zel'dovich approximation (Zel'dovich 1970) and the Lagrangian perturbation

theory, the linear Eulerian velocity field, Eq. (14), well describes the fluid displacement field even beyond the breaking point of the Eulerian linear perturbation theory.

The observed galaxy redshift is a composition of the cosmological redshift z and the Doppler shift sourced by galaxy peculiar velocities. It follows that converting the observed redshifts to comoving distances introduces a distortion along the line-of-sight (LOS). In the limit where linear theory is valid and the velocity component along the LOS satisfy $\mathbf{u}_{\parallel}/c \ll 1$, the comoving distance vector in redshift space, \mathbf{s} , reads

$$\mathbf{s} = \mathbf{r} + \frac{1+z}{H(z)}\mathbf{u}_{\parallel} = \mathbf{r} - \frac{f}{3}\Delta(r)\mathbf{r}_{\parallel}. \quad (15)$$

The last equality comes from the linear velocity field, Eq. (14). The relation between the real- and redshift-space VGCF can be derived considering the Jacobian of the real- to redshift-space mapping, Eq. (15),

$$\xi^s(\mathbf{s}) \simeq \xi(r) + \frac{f}{3}\Delta(r) + f\mu^2[\delta(r) - \Delta(r)], \quad (16)$$

where redshift-space quantities are labeled with the superscript s , and $\mu = r_{\parallel}/r$ is the cosine of the angle between the separation vector and the LOS (Cai et al. 2016; Hamaus et al. 2017, 2020, 2022). Assuming a linear bias relation that connects the observed galaxy density field to the underlying matter density field, we obtain a relation of the form $\xi(r) = b\delta(r)$, and consequently also $\bar{\xi}(r) = b\Delta(r)$ with $\bar{\xi}(r)$ being the average VGCF in a sphere of radius r . It follows that Eq. (16) becomes:

$$\xi^s(\mathbf{s}) \simeq \xi(r) + \frac{\beta}{3}\bar{\xi}(r) + \beta\mu^2[\xi(r) - \bar{\xi}(r)], \quad (17)$$

where $\beta = f/b$. Indeed, while generically the void-galaxy bias term b is not guaranteed to correspond to the standard galaxy large-scale effective bias, it is linearly related to it and converges to this value for sufficiently large voids (Sutter et al. 2014b; Pollina et al. 2017; Verza et al. 2022). This equation, together with Eq. (15), represents the theoretical model of the observed VGCF in redshift-space, according to linear theory. We note that the real-space quantities appearing in Eq. (17), i.e. $\xi(r)$ and $\bar{\xi}(r)$, are not directly observable. Since the real-space quantities are not known, we rely on the deprojection technique on the VGCF integrated along the LOS in redshift space, $\xi_p^s(s_{\perp})$ (Pisani et al. 2014; Hawken et al. 2017). The $\xi_p^s(s_{\perp})$ is identical to its real-space counterpart $\xi_p(r_{\perp})$, as $s_{\perp} = r_{\perp}$ and both are obtained by marginalizing over the LOS component, the one affected by RSD. So, with the forward Abel transform (N.

H. Abel 1842; Bracewell 1999) we obtain $\xi_p^s(s_{\perp})$ from $\xi^s(\mathbf{s})$:

$$\xi_p^s(s_{\perp}) = \int \xi^s(\mathbf{s}) ds_{\parallel} = 2 \int_{s_{\perp}}^{\infty} r \xi(r) (r^2 - s_{\perp}^2)^{-1/2} ds_{\perp}. \quad (18)$$

Then the inverse Abel transform (N. H. Abel 1842; Bracewell 1999) provides the inverse mapping from $\xi_p^s(s_{\perp})$ to get $\xi(r)$. This technique effectively allows to map $\xi_p^s(s_{\perp})$ into the 3D spherically symmetric VGCF in real-space:

$$\xi(r) = -\frac{1}{\pi} \int_r^{\infty} \frac{d\xi_p^s(s_{\perp})}{ds_{\perp}} (s_{\perp}^2 - r^2)^{-1/2} ds_{\perp}. \quad (19)$$

Following Hamaus et al. (2020, 2022), we adopted an empirically motivated modification of the model presented in Eq. (17), considering two nuisance parameters, \mathcal{M} and \mathcal{Q} . The modified version of the model is as follows:

$$\xi^s(\mathbf{s}) = \mathcal{M} \left\{ \xi(r) + \beta \bar{\xi}(r) + 2\mathcal{Q}\beta\mu^2[\xi(r) - \bar{\xi}(r)] \right\}, \quad (20)$$

and the mapping between coordinates in real and redshift space becomes:

$$r_{\perp} = s_{\perp} \quad r_{\parallel} = s_{\parallel} \left[1 - \mathcal{M} \frac{\beta}{3} \bar{\xi}(r) \right]^{-1}. \quad (21)$$

The parameter \mathcal{M} , a monopole-like term, acts as a free amplitude of the deprojected correlation function $\xi(r)$ in real space, compensating for potential biases introduced by the deprojection method and the possible contamination of the void sample by random Poisson fluctuations, which can suppress the monopole and quadrupole amplitudes (Cousinou et al. 2019). On the other hand, the parameter \mathcal{Q} , the quadrupole-like term, corrects for selection effects that can arise when voids are identified in the anisotropic redshift space (Pisani et al. 2015b; Correa et al. 2021, 2022). These effects, including shell-crossing and the virialization process, impact the structure of void boundaries in redshift space (Hahn et al. 2015), leading to the familiar Finger-of-God (FoG) effect (Jackson 1972). These distortions may influence the Jacobian terms in Eq. (17) and are part of the systematic effects that should be explored with further detail in future works.

So far, we have addressed the modeling of the VGCF in the presence of RSD alone. The AP effect, a geometric distortion, is modeled by expressing the fiducial coordinates, r^{fid} , in terms of the true coordinates, r^{true} . This coordinate transformation is applied using Eq. (8), which introduces the quantities q_{\parallel} and q_{\perp} ,

$$r_{\perp} = q_{\perp} s_{\perp} \quad r_{\parallel} = q_{\parallel} s_{\parallel} \left[1 - \mathcal{M} \frac{\beta}{3} \bar{\xi}(r) \right]^{-1}. \quad (22)$$

From this equation, we can obtain $r = \sqrt{r_{\parallel}^2 + r_{\perp}^2}$ and $\mu = r_{\parallel}/r$, entering in Eq. (20). As r_{\parallel} itself explicitly depends on the quantities we want to derive, it's possible to evaluate them by iteration of Eq. (22) (Hamaus et al. 2020, 2022). The combination of the q_{\parallel} and q_{\perp} parameters can be inferred from the eccentricity of the objects. To quantify this, it is useful to define the parameter linked to AP distortions, ϵ , as:

$$\epsilon \equiv \frac{q_{\perp}}{q_{\parallel}} = \frac{D_{\text{A}}^{\text{true}}(z)H^{\text{true}}(z)}{D_{\text{A}}^{\text{fid}}(z)H^{\text{fid}}(z)}. \quad (23)$$

If the fiducial cosmology matches the true one, then $\epsilon = 1$, and consequently, $r_{\parallel}^{\text{fid}} = r_{\parallel}^{\text{true}}$ and $r_{\perp}^{\text{fid}} = r_{\perp}^{\text{true}}$. Conversely, if a measurement of ϵ differs from 1, it indicates that the chosen fiducial cosmology deviates from the true one. In this scenario, we can use the parameter ϵ to constrain $D_{\text{A}}(z)H(z)$.

Following the VSF case, for this analysis we adopt three different cosmological models: Λ CDM, w CDM, and w_0w_a CDM. These models serve as our fiducial frameworks. The angular diameter distance, $D_{\text{A}}(z)$, and the Hubble parameter, $H(z)$, can be generalized with the following expressions (in the case of a flat universe):

$$D_{\text{A}}(z) = \int_0^z \frac{c}{H(z')} dz', \quad (24)$$

$$H(z) = H_0 \sqrt{\Omega_{\text{m}}(1+z)^3 + \Omega_{\text{de}}(1+z)^{3(1+w_0+w_a)} F(z)}, \quad (25)$$

where

$$F(z) = e^{-3w_a z/(1+z)}, \quad (26)$$

H_0 is the present-day Hubble constant, Ω_{m} is the matter density parameter, and Ω_{de} is the dark energy density parameter (with $\Omega_{\text{de}} \equiv \Omega_{\Lambda}$ in the Λ CDM model). The parameters w_0 and w_a describe the dark energy equation of state.

4.2. Likelihood analysis

In this sub-section we present measurements and the likelihood analysis of the VGCF. Those are performed using the *Voiager*⁷ publicly available package, which provides a pipeline to perform cosmological analyses using voids identified in large-scale structure survey data. This code measures dynamic and geometric shape distortions in void stacks and propagates the measurement down to constraints on cosmological parameters using Bayesian inference.

The data vector is represented by the VGCF measured in redshift space. As thoroughly discussed in Section 4.1, this function is anisotropic along the LOS, and

is therefore two-dimensional, $\xi^s(s_{\perp}, s_{\parallel})$. By re-writing the s_{\perp} and s_{\parallel} quantities in term of s and $\mu_s = s_{\parallel}/s$, it is possible to decompose the VGCF into multipoles of the Legendre polynomials \mathcal{P}_{ℓ} of order ℓ :

$$\xi_{\ell}^s(s) = \frac{2\ell+1}{2} \int_{-1}^1 \xi^s(s, \mu_s) \mathcal{P}_{\ell}(\mu_s) d\mu_s. \quad (27)$$

The monopole, ξ_0 , represents the average galaxy density profile within the void region. The quadrupole, ξ_2 , is identically null for statistically isotropic samples. Any deviation from zero indicates anisotropy: a positive quadrupole means the void density profile is compressed along the LOS, while a negative quadrupole suggests elongation along the LOS. Similarly, a non-zero hexadecapole, ξ_4 , indicates a breakdown of statistical isotropy. We note, however, that in linear theory this quantity is expected to be identically null, Eq. (17), therefore its interpretation in terms of distortions of the void shape involves higher-order effects.

Even if the multipole decomposition provides a clear physical interpretation, actually for VGCF analyses it is possible to rely on either the 2D cross-correlation function $\xi^s(s_{\perp}, s_{\parallel})$ for model fitting with coordinates along and perpendicular to the LOS (this will, of course, include information on both RSD and AP), or on the decomposition into multipoles of the Legendre polynomials. Here we use the 2D cross-correlation function, since this provides a better balance for the number of bins that sample the inner core of voids with respect to the bins sampling the slope of the void profile (inner bins are more strongly impacted by noise in e.g., the deprojection), but we also provide the multipoles corresponding to $\ell = 0, 2, 4$, for completeness.

For our estimation of the VGCF $\xi^s(s_{\perp}, s_{\parallel})$ we use the Landy-Szalay estimator (Landy & Szalay 1993):

$$\xi^s(s_{\perp}, s_{\parallel}) = \frac{\langle \mathcal{D}_{\text{v}} \mathcal{D}_{\text{g}} \rangle - \langle \mathcal{D}_{\text{v}} \mathcal{R}_{\text{g}} \rangle - \langle \mathcal{R}_{\text{v}} \mathcal{D}_{\text{g}} \rangle + \langle \mathcal{R}_{\text{v}} \mathcal{R}_{\text{g}} \rangle}{\langle \mathcal{R}_{\text{v}} \mathcal{R}_{\text{g}} \rangle}. \quad (28)$$

The angled brackets denote normalized pair counts of void-center v and galaxy, g, positions. The letter \mathcal{D} refers to the data while \mathcal{R} refers to the random positions. The pair counts are binned in s_{\perp} and s_{\parallel} . We implemented a fixed binning scheme based on the effective void radius for each individual void, expressing all distances in units of the void radius R_{eff} . Normalizing the void-galaxy distance with respect to the void radius is crucial to coherently overlap regions of similar density, and to enhance the topology of voids, such as the compensation wall, making our observable ideal to extract cosmological information (Hamaus et al. 2014, 2017, 2020, 2022). The catalogs of random voids and

⁷ <https://voiyager.readthedocs.io>

galaxies is characterized by the same redshift dependence of the distributions of voids and galaxies, respectively, as measured in the simulated lightcone, except for the normalization, given by the total number of objects. In particular, we prepared random void catalogs by considering a number of random voids much larger than the corresponding number of voids measured in the simulated lightcone. Moreover, the random catalogs share the same angular footprint as the corresponding void and galaxy catalogs from the lightcone. For the catalog of random voids we also applied to each void center an effective radius, randomly taken from the radius distribution of voids in the lightcone.

The covariance matrix:

$$\mathbf{C}_{ij} = \langle (\xi^s(\mathbf{s}_i) - \langle \xi^s(\mathbf{s}_i) \rangle) (\xi^s(\mathbf{s}_j) - \langle \xi^s(\mathbf{s}_j) \rangle) \rangle, \quad (29)$$

quantifies the uncertainty of the measured VGCF $\xi^s(s_\perp, s_\parallel)$. In this equation, angled brackets denote the ensemble average of measurements. Since we lack various mock catalog realizations, we estimate the covariance matrix, \mathbf{C}_{ij} , via the jackknife technique. This methodology relies on ergodicity, which allows us to average measurements across different spatial patches to estimate the covariance matrix. The jackknife method is implemented by measuring ξ^s through Eq. (28) several times, by excluding one (non-overlapping) void at a time. In this way we obtain N_v samples, where N_v is the total number of voids, to estimate the corresponding covariance \mathbf{C}_{ij} . This methodology has undergone testing on simulations and validation on mocks in prior analyses (Paz et al. 2013; Cai et al. 2016; Correa et al. 2019; Hamaus et al. 2020, 2022; Degni et al. in prep). We note that previous work showed that the Hartlap correction (Hartlap et al. 2007) is expected to be negligible (of a few percent level, see Hamaus et al. 2022), given the number of subsamples, N_v . It has been demonstrated that, in the limit of large sample sizes, the jackknife technique produces consistent covariance estimates compared to those derived from numerous independent mock catalogs (Favole et al. 2021). Any residual discrepancies between the two methods suggest a slight overestimation of covariances by the jackknife approach, thereby rendering our error forecast conservative.

From the data vector of Eq. (28), and the theoretical model from Eqs. (20) and (22), we can express the corresponding Gaussian likelihood $L(\hat{\xi}^s|\Theta)$ of the data $\hat{\xi}^s$ considering the model parameter vector $\Theta = (\beta, \epsilon, \mathcal{M}, \mathcal{Q})$ as:

$$\ln L(\hat{\xi}^s|\Theta) = -\frac{1}{2} \sum_{i,j} \left(\hat{\xi}^s(\mathbf{s}_i) - \xi^s(\mathbf{s}_i|\Theta) \right) \mathbf{C}_{ij}^{-1} \left(\hat{\xi}^s(\mathbf{s}_j) - \xi^s(\mathbf{s}_j|\Theta) \right). \quad (30)$$

We evaluate the posterior probability distribution by running MCMC analyses with publicly available **emcee** (Foreman-Mackey et al. 2019) Python package. We can assess the quality of the maximum-likelihood model (best fit) relying on the evaluation of the reduced χ^2 statistic:

$$\chi^2 = -\frac{2}{N_{\text{dof}}} \ln L(\hat{\xi}^s|\Theta), \quad (31)$$

where the number of degrees of freedom is $N_{\text{dof}} = N_{\text{data}} - N_{\text{par}}$, with N_{data} the number of bins and N_{par} the number of free parameters.

In each redshift bin, the data array $\xi^s(s_\perp, s_\parallel)$ is measured in bins of s_\perp and s_\parallel . We consider 18 equispaced bins in each of the two dimensions, resulting in $N_{\text{bin}} = 18 \times 18 = 324$ bins. It follows that $N_{\text{dof}} = 320$ in each of the considered redshift bins, as $N_{\text{par}} = 4$. On the one hand this number is much lower than the number of voids per redshift bin considered, therefore guaranteeing enough statistics for a robust estimate of the corresponding covariance matrix, Eq. (29); on the other hand, N_{bin} is large enough to resolve the features of the 2D VGCF.

4.3. Results

The VGCF analysis was conducted using the void sample extracted with **VIDE**, a total of $N_v = 82551$ voids, divided into three redshift bins of equal number of voids each, as explained in Section 2. Specifically, for the study of the VGCF, the voids underwent post-processing, where a purity cut was applied to avoid the inclusion of spurious Poissonian voids. The cut follows:

$$R_{\text{eff}} > N_s \left(\frac{4\pi}{3} n_g(Z) \right)^{-1/3}, \quad (32)$$

where Z represents the redshift of void centers, and the parameter N_s sets the minimum void size in units of the average tracer separation. A void catalog with a low N_s value may be prone to stronger spurious void contamination, i.e. voids misidentified due to the sparsity of tracers, Fingers-of-God, or other systematic effects (Neyrinck 2008; Pisani et al. 2015b; Cousinou et al. 2019; Correa et al. 2021, 2022). On the other hand, a high N_s value can drastically reduce the statistical relevance of the void sample. Choosing the optimal N_s is a trade off between these two effects. In this VGCF analysis, we adopt $N_s = 3$, resulting in a final sample of $N_v = 67158$ voids with a minimum effective radius of $8.0 h^{-1} \text{Mpc}$.

To compute the model for the likelihood analysis via Eqs. (20) and (22), it is essential to determine the stacked density profile or VGCF in real-space, $\xi(r)$. This can be achieved using the deprojection technique outlined in Section 4.1.

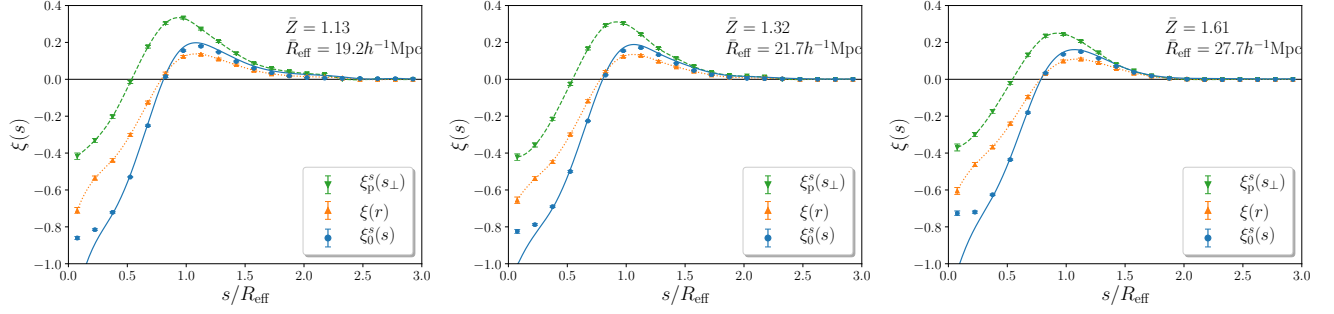


Figure 6. Projected void-galaxy cross-correlation function $\xi_p^s(s_\perp)$ in redshift space (green wedges, interpolated with dashed line) and its real-space counterpart $\xi(r)$ in 3D after deprojection (orange triangles interpolated with dotted line). The redshift-space monopole $\xi_0^p(s)$ (blue dots) and its best-fit model based on Eqs. (20) and (22) are shown for comparison (solid line). Adjacent bins in redshift increase from left to right, with mean void redshift, \bar{Z} , and effective radius, \bar{R}_{eff} , as indicated in each panel.

We use **Voiager** to compute the LOS integration of $\hat{\xi}^s(s_\perp, s_\parallel)$ obtaining $\xi_p^s(s_\perp)$. From this quantity we then obtain $\xi(r)$ via the deprojection technique, Eq. (19). Integration are performed by interpolating both $\xi_p^s(s_\perp)$ and $\xi(r)$ with a cubic spline. Figure 6 illustrates the results for $\xi(r)$ (orange triangles interpolated with dotted line) for each of the three redshift bins, together with the projected void-galaxy cross-correlation function $\xi_p^s(s_\perp)$ in redshift space (green wedges, interpolated with dashed line) and the redshift-space monopole $\xi_0^p(s)$ (blue dots) with its best-fit model (blue solid line) based on Eqs. (20) and (22), which is shown for comparison. The statistical noise that could be introduced by the deprojection technique is minimal, due to the large number of voids. However, some residual noise is observed in the innermost bins, where separations from the void center are small and tracers are also sparser, which affects the accuracy of the deprojection and the subsequent spline interpolation (Pisani et al. 2014; Hamaus et al. 2020). Consequently, we omit the first radial bin from our model fits. To calculate the model for $\xi(r)$ with the deprojection technique, we rely on the data, which introduces its own covariance, leading to a correlation with $\hat{\xi}^s(s)$. Nevertheless, the model considered, Eq. (20), considers the amplitude of the VGCF as a free parameter, \mathcal{M} . The results are therefore conservative, since any correlation between data and model would reduce the total covariance in our likelihood estimation. Besides the deprojection technique presented here, other methods can be used to obtain the $\xi(r)$ in real space. Other studies employ a numerical model based on the measurements of the monopole obtained from simulated data in real space, where available (Nadathur et al. 2020b; Radinović et al. 2023). Alternatively, theoretical models could also be used (Verza et al. 2024). By using theoretical models, we could eliminate the potential dependence on the cosmology of the mock

data, which would otherwise be introduced when relying on mocks to compute the real-space model. On the one hand the use of a full theoretical model can increase the constraining power; on the other hand the model-free methodology explored in this analysis ensures its robustness, as it is less affected by biases related to unknown systematic effects or potential dependencies on the cosmology of the mock data.

The data vector in redshift space is constructed using the 2D VGCF, $\xi^s(s_\perp, s_\parallel)$, estimated with the Landy-Szalay estimator. The measurements are performed across three different redshift bins, as presented in Section 2. The resulting VGCF, along with the corresponding multipoles (dots, triangles, and wedges), are shown in Figure 7. We conducted a full MCMC analysis to fit the model described by Eqs. (20) and (22) obtaining the posterior distribution for the model parameters $\Theta = [f/b, \epsilon, \mathcal{M}, \mathcal{Q}]$ as illustrated in Figure 8. For each MCMC analysis we explore 16 walkers. We then post-process the chains by removing the first 10% of the steps. To ensure that different steps are uncorrelated, we consider one chain-step every $\tau_{\text{max}}/2$, where τ_{max} is the maximum value of the multi-dimensional time-covariance of the chain, computed with the Goodman & Weare (2010) estimator. The resulting length of the chains in the three redshift bins is $\sim 4 \times 10^5$. This resulted in a reduced $\chi^2 = 1.97, 1.20, 1.04$ in the three redshift bins, respectively.

We note that the VGCF is sensitive to the growth rate of cosmological perturbations via f/b and to the expansion history of the universe via ϵ . This observable is also sensitive to other cosmological parameters, such as σ_8 and h . However, the ability to constrain these other quantities depends on the specific VGCF model. In this work we considered a model-independent approach, which exclusively probes a subset of background parameters in a robust and unbiased way, through the AP test.

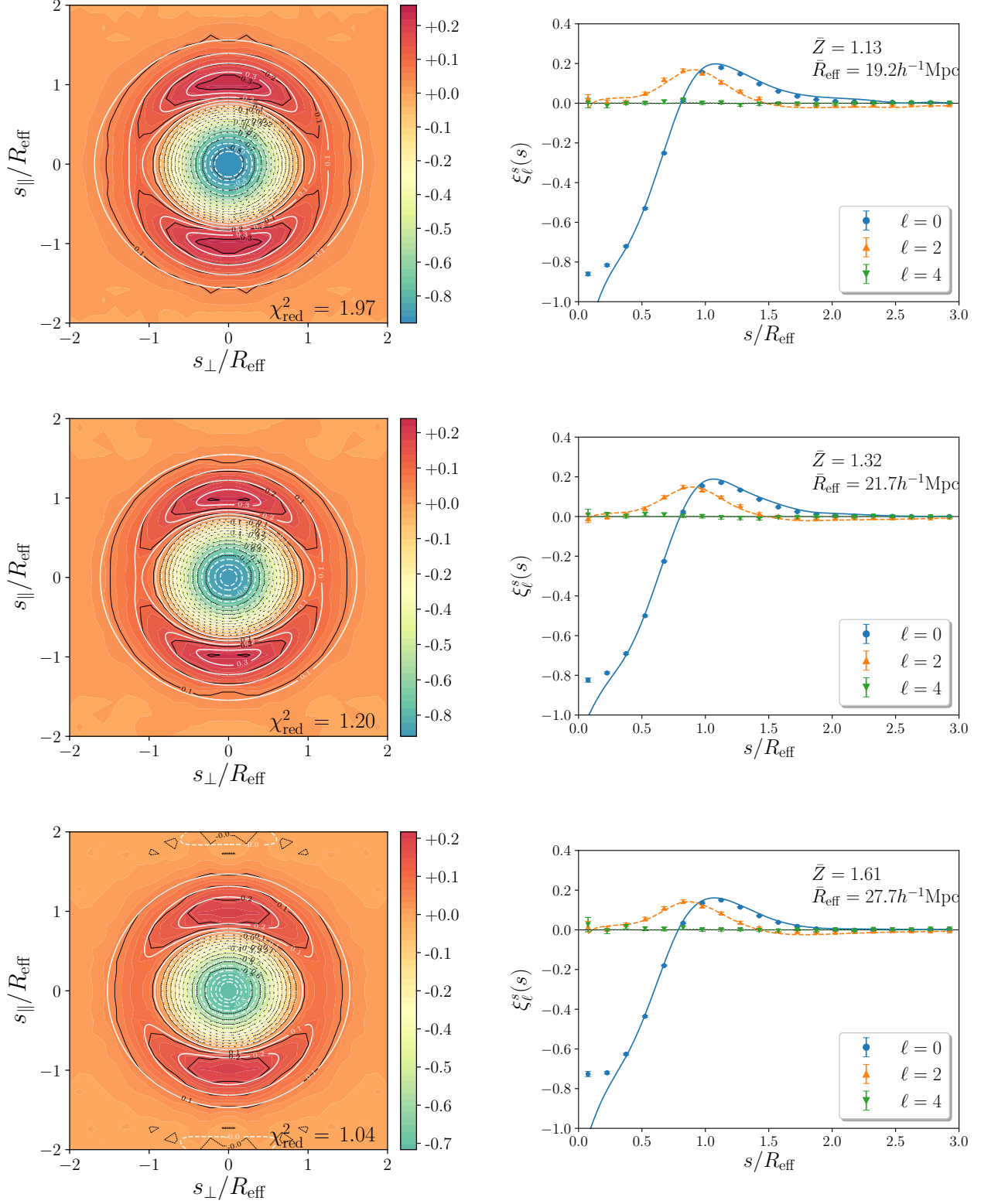


Figure 7. Void-galaxy cross-correlation function in redshift space. Left: $\xi^s(s_\perp, s_\parallel)$ in 2D (color scale with black contours) and best-fit model from Eqs. (20) and (22) (in white contours). Right: monopole (blue dots), quadrupole (orange triangles) and hexadecapole (green wedges) of $\xi^s(s_\perp, s_\parallel)$ with their best-fit model (solid, dashed, dotted lines). The mean void redshift, \bar{Z} , and effective radius, \bar{R}_{eff} , of each redshift bin are indicated.

The best-fit models are shown as white contours in the 2D VGCF plots in Figure 7. For reference, the corresponding multipole models are also plotted. The best-fit models appear to represent the data well down to small scales. Our results exhibit correlations consistent with those found by Hamaus et al. (2020) and Hamaus et al. (2022). Specifically, we observe a weak correlation between ϵ and β , and a strong correlation between β and \mathcal{M} . The estimated true values, represented by dashed lines in Figure 8, are computed as follows. To compute the true value of β , both the values for $f(z)$ and $b(z)$ are required. The growth rate f is computed via

$$f(z) \simeq \left[\frac{\Omega_m(1+z)^3}{H^2/H_0^2} \right]^\gamma, \quad (33)$$

with a growth index $\gamma \simeq 0.55$ (Lahav et al. 1991; Linder 2005). For the bias $b(z)$ we assume the relation in Wang et al. (2022). The parameter ϵ is expected to be equal to 1, as we used the cosmology of the simulation to convert angles and redshifts into distances, introducing no AP effect. The parameters \mathcal{M} and \mathcal{Q} do not have specific values, and their distribution is not relevant to the cosmological interpretation of the posteriors (given their use to account for potential biases due to e.g., spurious voids contamination and noise in the deprojection).

The relative precision of both β and ϵ varies across the redshift bins, with values ranging from 6.4% to 6.8% for β and from 0.7% to 0.9% for ϵ . Notably, ϵ is measured with high precision and accuracy in all redshift bins, with deviations of only $0.1\sigma_\epsilon$ to $0.3\sigma_\epsilon$ from its true value. We note that for f/b some discrepancies may arise—observable here thanks to the high statistical power of the Roman void sample leading to tight error bars—and that could lead to biases in the inferred $f\sigma_8$ due to two reasons. First, the bias parameter can be different from its large-scale counterpart (obtained with galaxies two-point correlation function or power spectrum computations, see Section 4.1), especially in small voids (Pollina et al. 2017; Verza et al. 2022). In this case the linear bias approximation could still be valid, but the linear relation may be verified with a different slope. Second, projection effects in the parameter space, due to the strong degeneracy between f/b and \mathcal{M} , can affect the inferred value of $f\sigma_8$. It is important to note that these deviations in β do not significantly affect the overall quality of the fit. This is primarily due to the role played by the nuisance parameters \mathcal{M} and \mathcal{Q} , which help to mitigate the impact of the deviations in β without substantially influencing the precision or accuracy of ϵ .

From the posteriors of $\beta \equiv f/b$ and $\epsilon \equiv q_\perp/q_\parallel$, it is possible to derive constraints on $f\sigma_8$ and $D_A H$. For

the former, we assume that $\xi(r)$ is proportional to $b\sigma_8$, and thus we multiply f/b by the underlying value of $b\sigma_8$ provided by the mock. Additionally, we assume that the relative precision on f/b and $f\sigma_8$ is the same. Furthermore, we neglect the dependence on h , which enters into the definition of σ_8 and should ideally be marginalized over (Sánchez 2020). For the latter case, we compute $D_A H$ by multiplying ϵ by the fiducial $D_A H$, following Eq. (23). We summarize all the results in Table 3. As expected, the discrepancies observed in the values of β in the second and third redshift bins propagate to the estimated values of $f\sigma_8$.

The measurements of $f\sigma_8$ and $D_A H$ as a function of redshift can be used to constrain cosmological models, for example, by inverting Eqs. (24) and (25). As in the analysis of the VSF, we explore three different cosmological models. The first model is the Λ CDM model, where the parameter space is $\Theta = [\Omega_m]$, probed by the AP test. We use flat priors for Ω_m in the range (0.15, 0.65). The second model is the w CDM model, with parameters $\Theta = [\Omega_m, w]$, combining the Λ CDM priors with a flat prior on w in the range $(-3, 2)$. The third model is the $w_0 w_a$ CDM model, with parameters $\Theta = [\Omega_m, w_0, w_a]$, and flat priors identical to those of w CDM, along with w_a in the range $(-8, 5)$.

Figure 9 shows the 2D projected posterior distributions of the cosmological models explored: Λ CDM (blue), w CDM (orange), and $w_0 w_a$ CDM (green). The shaded regions represent the 68% confidence level, while the outer contours indicate the 95% confidence level. The true values of the parameters are marked by gray dashed lines. Table 4 lists the best-fit values and the 1D 68% confidence intervals for each cosmological parameter in each model. In a Λ CDM model, the one assumed for the simulation, we recover the value of Ω_m with a precision of $\simeq 3\%$ that lays in a 0.1σ interval from the true value. In the second scenario, a w CDM model, Ω_m is estimated with a precision of $\simeq 6.6\%$ and its distance from the true value is 0.3σ . The third and final scenario, the $w_0 w_a$ CDM model, is more complex, leading to larger uncertainties and making the best-fit values more challenging to estimate from the posteriors. Typically in future analyses a wider redshift range, more redshift bins, and/or probe combination can break degeneracies. Moreover, in future studies, we should account for projection effects in the posterior distribution (Raveri et al. 2024).

To conclude this section, it is worth mentioning that we have relied on the method presented by Hamaus et al. (2020), that significantly improves the constraining power of the VGCF. For a more conservative forecast we have allowed the parameters \mathcal{M} and \mathcal{Q} to vary.

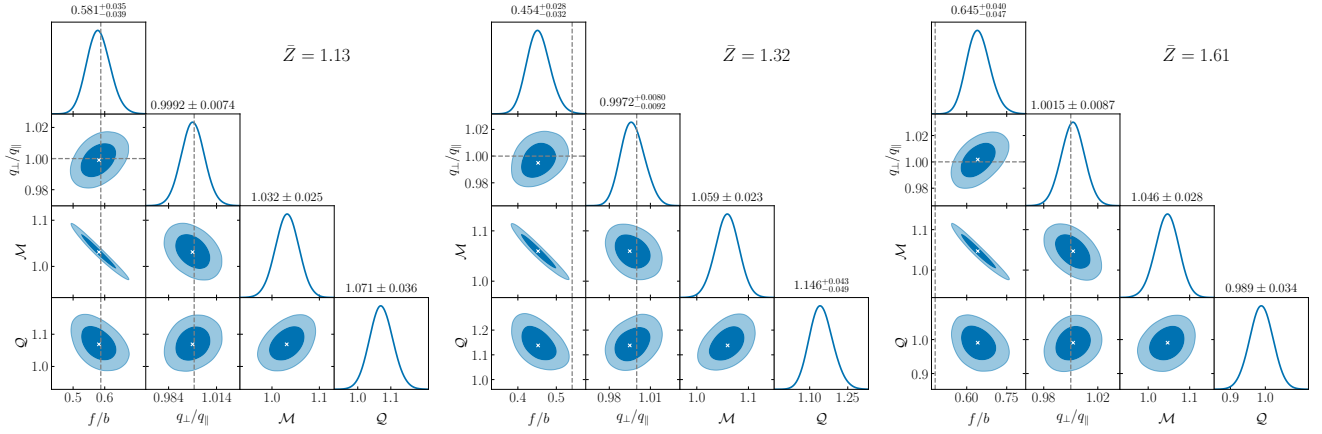


Figure 8. VGCF: posterior probability distribution of the model parameters that enter in Eqs. (20) and (22), obtained via MCMC from the data shown on the left of Figure 7. Dark and light-shaded areas represent the 68% and 95% CL, with a cross marking the best fit, dashed lines indicate fiducial values of the RSD and AP parameters. The top of each column states the mean and standard deviation of the 1D marginal distributions. Adjacent bins in void redshift with mean value \bar{Z} increase from left to right, as indicated.

| \bar{Z} | b | $\epsilon \pm \sigma_\epsilon$ | $\beta \pm \sigma_\beta$ | $f\sigma_8 \pm \sigma_{f\sigma_8}$ | $D_A H/c \pm \sigma_{D_A H/c}$ |
|-----------|-------|--------------------------------|--------------------------|------------------------------------|--------------------------------|
| 1.13 | 1.518 | 0.999 ± 0.007 | 0.581 ± 0.037 | 0.413 ± 0.026 | 1.607 ± 0.012 |
| 1.32 | 1.687 | 0.997 ± 0.009 | 0.454 ± 0.031 | 0.333 ± 0.022 | 1.980 ± 0.017 |
| 1.61 | 1.945 | 1.001 ± 0.009 | 0.645 ± 0.044 | 0.489 ± 0.033 | 2.622 ± 0.023 |

Table 3. VGCF: forecasted constraints on RSD and AP parameters ϵ , β , $f\sigma_8$, and $D_A H/c$ (mean values with 68% CL). Results are given in three redshift bins with mean \bar{Z} , and large-scale galaxy bias b .

| Model | Ω_m | w_0 | w_a |
|---------------|---------------------------|-------------------------|------------------------|
| Λ CDM | $0.308^{+0.007}_{-0.009}$ | -1 | 0 |
| w CDM | $0.303^{+0.013}_{-0.015}$ | $-1.05^{+0.25}_{-0.27}$ | 0 |
| $w_0 w_a$ CDM | $0.295^{+0.215}_{-0.070}$ | $-1.06^{+1.80}_{-0.44}$ | $1.04^{+0.70}_{-6.64}$ |

Table 4. VGCF: forecasted constraints on cosmological parameters, Ω_m , w_0 , and, w_a , estimated assuming three different cosmological models: Λ CDM, w CDM, and $w_0 w_a$ CDM.

While leaving those parameters free to vary is a conservative option, we notice here that the full power of the method can be reached by fixing those parameters, that is when a better understanding of spurious voids and other aforementioned effects is obtained. Further tests to increase our understanding of such parameters, which we aim to conduct in future studies, include the study of the dependence of \mathcal{M} and \mathcal{Q} on the cosmological and structure formation models assumed in the mocks (e.g., on the modelling of galaxy properties). Alternatively, for tighter constraints it is possible to rely on a set of mocks to calibrate the values of \mathcal{M} and \mathcal{Q} that can then be held fixed during the analysis, at the expense of trusting the features of the mocks used for calibration. Given these points, until a better understanding

is reached, calibrated results should be considered less robust; therefore, we do not explore the possibility of calibrating them here.

5. DISCUSSION AND CONCLUSION

In this work we present a comprehensive cosmological forecast from void statistics to be measured in the Roman reference HLSS survey. We build void catalogs relying on a Roman-like mock and employ state of the art models to extract cosmological constraints from the VSF and VGCF. Our results showcase an impressive constraining power from both statistics. The full power of the different void statistics can be confirmed by considering voids' probe combination, as the two statistics explored here respond differently to cosmology. The VSF is sensitive to both the cosmological fluctuations, through the linear matter power-spectrum, and the background expansion of the Universe (see Sections 3.2–3.4). The VGCF is a sensitive probe of the expansion history of the universe, through the AP test. Previous work suggests that the covariance between the VSF and the VGCF is low (Kreisch et al. 2022; Contarini et al. 2024), therefore the constraining power of the joint analysis can be safely estimated by combining the two independent posterior distributions. To showcase the

| Model | | Ω_m | σ_8 | h | w_0 | w_a |
|---------------|-------|------------------------------|------------------------------|------------------------------|----------------------------|-------------------------|
| True | | 0.3089 | 0.8147 | 0.6774 | -1 | 0 |
| Λ CDM | opt. | $0.3086^{+0.0077}_{-0.0080}$ | $0.8145^{+0.0258}_{-0.0272}$ | $0.6764^{+0.0164}_{-0.0168}$ | -1 | 0 |
| | pess. | $0.3100^{+0.0066}_{-0.0093}$ | $0.8212^{+0.0211}_{-0.0336}$ | $0.6726^{+0.0212}_{-0.0147}$ | -1 | 0 |
| w CDM | opt. | $0.3095^{+0.0052}_{-0.0124}$ | $0.8167^{+0.0186}_{-0.0392}$ | $0.6757^{+0.0215}_{-0.0144}$ | $-1.023^{+0.171}_{-0.113}$ | 0 |
| | pess. | $0.3089^{+0.0063}_{-0.0121}$ | $0.8149^{+0.0226}_{-0.0389}$ | $0.6801^{+0.0189}_{-0.0208}$ | $-1.041^{+0.195}_{-0.101}$ | 0 |
| w_0w_a CDM | opt. | $0.3238^{+0.0250}_{-0.0262}$ | $0.8601^{+0.0721}_{-0.0864}$ | $0.6584^{+0.0246}_{-0.0297}$ | $-0.934^{+0.216}_{-0.182}$ | $-0.47^{+0.93}_{-0.93}$ |
| | pess. | $0.3313^{+0.0247}_{-0.0310}$ | $0.8760^{+0.0780}_{-0.0990}$ | $0.6563^{+0.0337}_{-0.0370}$ | $-0.904^{+0.240}_{-0.208}$ | $-0.97^{+1.38}_{-1.23}$ |

Table 5. Combination of the VGCF and VSF: maximum posterior distribution values and 1D 68% CL interval of the cosmological parameters explored for each considered cosmological model (we show both the optimistic and pessimistic scenarios).

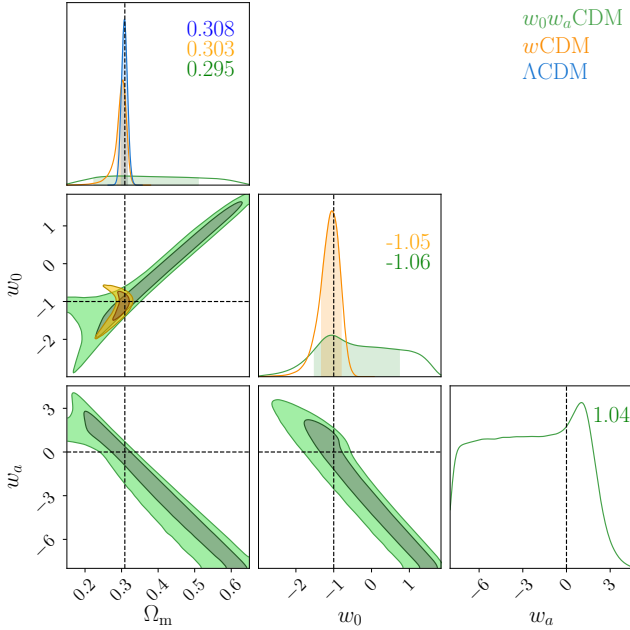


Figure 9. VGCF: expected constraints on Ω_m , w_0 , and w_a for the three different cosmologies tested here. In blue we show the Λ CDM model, while orange and green correspond to w CDM and w_0w_a CDM respectively. Dashed lines indicate the true values. Numbers in color correspond to the estimated values for the parameters, for the different cosmological models.

constraining power of a joint void-analysis, Figures 10 and 11 represent the overlapping forecast contours for the cosmological models and parameters explored in this work, considering the optimistic case for the VSF. We list in Table 5 the best-fit value and 1D 68% CL for each cosmological parameter from the joint distribution, for both the optimistic and pessimistic scenario. The right panel of Figure 10 shows the Λ CDM case, with the pro-

jected 2D posterior distribution of the VSF in blue, the VGCF in orange, and the combined posterior distribution in dark gray. It should be noted that the narrower posterior distribution for Ω_m in the VGCF case leads to a tightening of constraints even for parameters that are not probed by the VGCF, i.e. σ_8 and h (or H_0). The same observation is valid also for the w CDM case, Figure 10 left panel. Moreover, it is important to notice the different orientation, i.e. the complementarity, in the $w - \Omega_m$ plane. For the w_0w_a CDM case, shown in Figure 11, the situation is inverted. The VGCF, probing the background expansion of the Universe, shows wider contours, in particular for Ω_m . The corresponding VSF posterior distribution shows a higher constraining power, probably due to the fact that, together with its impact on the expansion history of the Universe, the dark energy equation of state also affects the growth of structure, i.e. σ_8 , to which the VSF is directly sensitive, while the AP test, performed with the VGCF, is not. Additionally, we wish to notice that, while selecting three bins is an effective choice for the analysis of the VGCF when considering the w CDM case, it may be harder to break degeneracies with three bins when considering the w_0w_a CDM case. Nevertheless, the combination of the VSF and the VGCF shows an interesting complementarity for Ω_m and the dark energy parameters, w_0 and w_a , leading to strong constraints for the dynamical dark energy parameters as well.

In future works, when combining the various void statistics, we plan to rely on mock catalogs spanning various cosmological realizations and to consider various galaxy-halo connection models, such as SAM, halo-occupation distribution (HOD), and sub-halos matching techniques (SHAM), and spanning the corresponding parameters. This will allow to properly model the

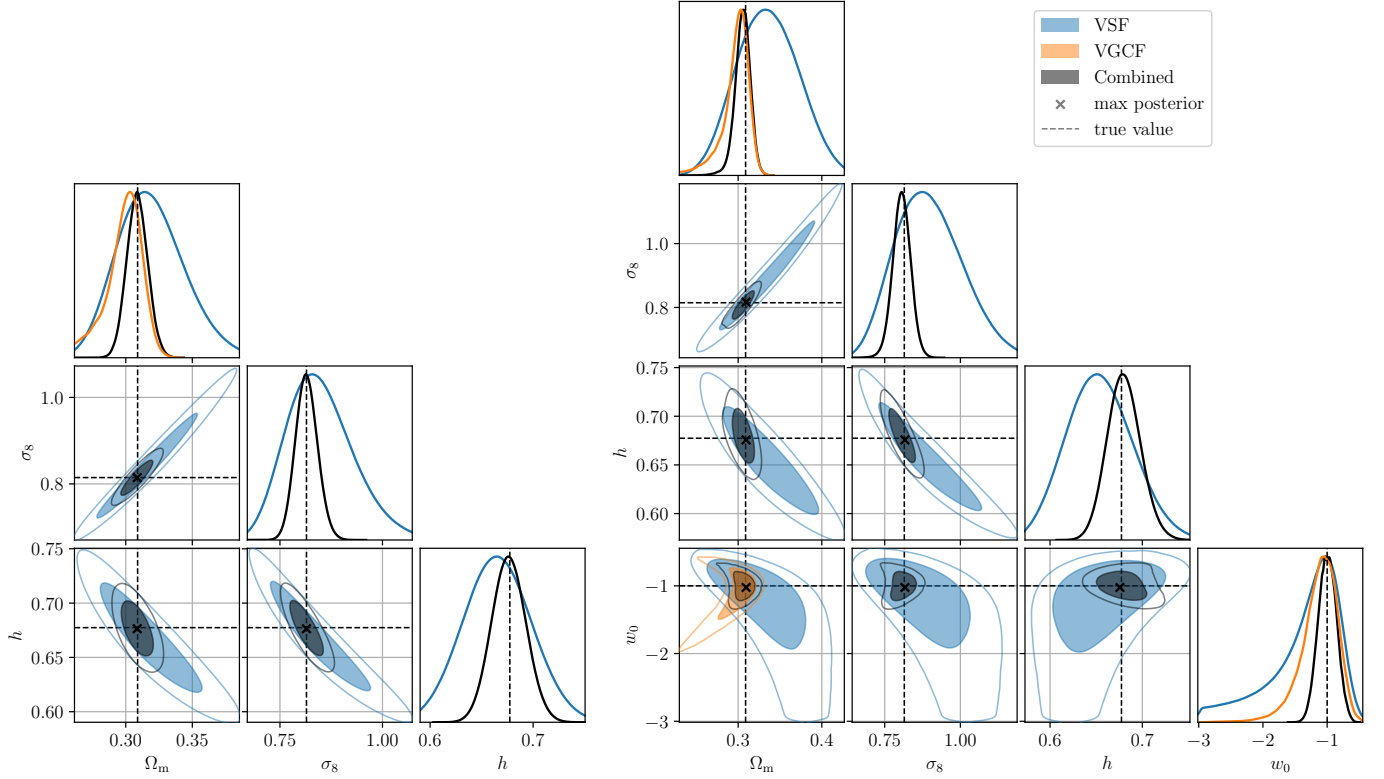


Figure 10. Combination of the VGCF and VSF: posterior distributions of the cosmological parameters explored in the Λ CDM (left) and the w CDM model (right), obtained from the VSF (blue), VGCF (orange), and combining the two statistics (dark gray). The filled internal region shows the 68% CL, the outer line shows the 95% CL. Black dashed lines indicate the true values, crosses correspond to the maximum of the posterior distributions.

covariance, for both the VSF, the VGCF, and the cross-covariance, modelling the cosmological dependence and marginalizing over galaxy properties, represented by the galaxy-halo connection models. Crucially, we expect the use of mock galaxy catalogs to allow a better understanding of the free parameters of our models, such as the redshift and tracer dependency for the VSF effective barrier in Eq. (5), and the nuisance parameters \mathcal{M} and \mathcal{Q} for the VGCF model in Eq. (20). Such understanding, together with the increase in the constraining power for both statistics, will enhance the robustness of our models, alongside with accounting for observational effects (e.g., through the use of realistic survey masks). In the current cosmology landscape, if dynamical dark energy is confirmed (DESI Collaboration et al. 2024), the community will focus on pinning down the dark energy equation of state, and Roman voids are expected to be a powerful, independent probe in this context. With a first, comprehensive analysis of a Roman-like mock, this work paves the way to using Roman voids to inde-

pendently constrain cosmological parameters with tight precision.

GV acknowledges NASA grant EUCLID12-0004. GV and AP acknowledge support from the Simons Foundation to the Center for Computational Astrophysics at the Flatiron Institute. AP acknowledges support from the European Research Council (ERC) under the European Union’s Horizon programme (COSMOBEST ERC funded project, grant agreement 101078174), as well as support from the french government under the France 2030 investment plan, as part of the Initiative d’Excellence d’Aix-Marseille Université - A*MIDEX AMX-22-CEI-03. YW’s work is funded in part by NASA grant #80NSSC24M0021. Part of this work was done at Jet Propulsion Laboratory, California Institute of Technology, under a contract with the National Aeronautics and Space Administration (80NM0018D0004). The authors are grateful to Shirley Ho and David Spergel for useful discussions. This paper relies on the public code *Voiager*⁸.

⁸ <https://voiyager.readthedocs.io/>

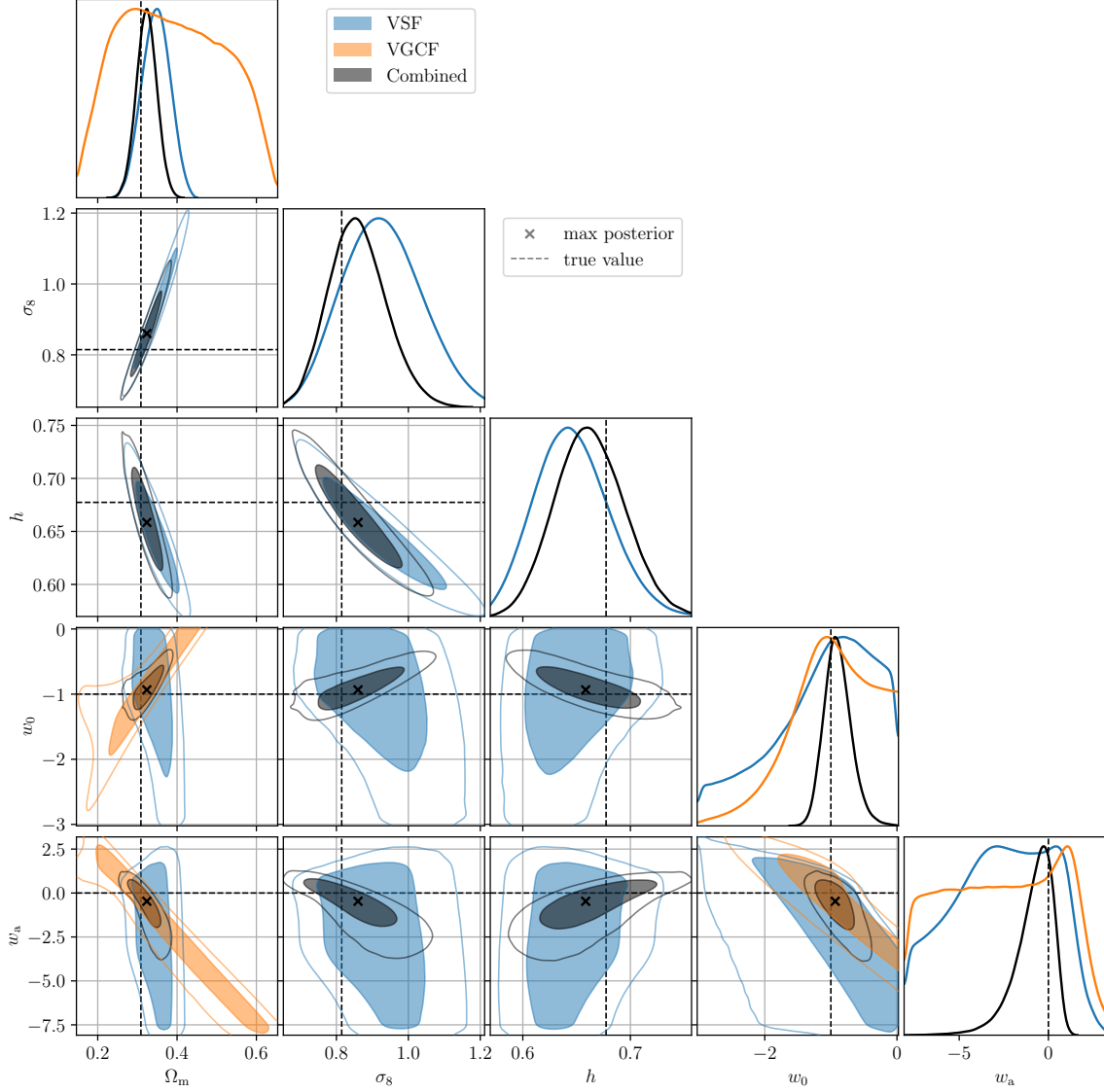


Figure 11. Combination of the VGCF and VSF: posterior distributions of the cosmological parameters explored in the w_0w_a CDM model, obtained from the VSF (blue), VGCF (orange), and combining the two statistics (dark gray). The plot is organized as Fig 10.

REFERENCES

- Abel, T., Hahn, O., & Kaehler, R. 2012, MNRAS, 427, 61, doi: [10.1111/j.1365-2966.2012.21754.x](https://doi.org/10.1111/j.1365-2966.2012.21754.x)
- Achitouv, I. 2019, PhRvD, 100, 123513, doi: [10.1103/PhysRevD.100.123513](https://doi.org/10.1103/PhysRevD.100.123513)
- Achitouv, I., Blake, C., Carter, P., Koda, J., & Beutler, F. 2017, PhRvD, 95, 083502, doi: [10.1103/PhysRevD.95.083502](https://doi.org/10.1103/PhysRevD.95.083502)
- Alcock, C., & Paczynski, B. 1979, Nature, 281, 358, doi: [10.1038/281358a0](https://doi.org/10.1038/281358a0)
- Aubert, M., Cousinou, M.-C., Escoffier, S., et al. 2022, MNRAS, 513, 186, doi: [10.1093/mnras/stac828](https://doi.org/10.1093/mnras/stac828)
- Bardeen, J. M., Bond, J. R., Kaiser, N., & Szalay, A. S. 1986, ApJ, 304, 15, doi: [10.1086/164143](https://doi.org/10.1086/164143)
- Bayer, A. E., Liu, J., Kreisch, C. D., & Pisani, A. 2024, PhRvD, 110, L061305, doi: [10.1103/PhysRevD.110.L061305](https://doi.org/10.1103/PhysRevD.110.L061305)
- Bayer, A. E., Villaescusa-Navarro, F., Massara, E., et al. 2021, ApJ, 919, 24, doi: [10.3847/1538-4357/ac0e91](https://doi.org/10.3847/1538-4357/ac0e91)
- Benson, A. J. 2012, NewA, 17, 175, doi: [10.1016/j.newast.2011.07.004](https://doi.org/10.1016/j.newast.2011.07.004)

- Beyond-2pt Collaboration, :, Krause, E., et al. 2024, arXiv e-prints, arXiv:2405.02252, doi: [10.48550/arXiv.2405.02252](https://doi.org/10.48550/arXiv.2405.02252)
- Biswas, R., Alizadeh, E., & Wandelt, B. D. 2010, *PhRvD*, 82, 023002, doi: [10.1103/PhysRevD.82.023002](https://doi.org/10.1103/PhysRevD.82.023002)
- Bond, J. R., Cole, S., Efstathiou, G., & Kaiser, N. 1991, *ApJ*, 379, 440, doi: [10.1086/170520](https://doi.org/10.1086/170520)
- Bonici, M., Carbone, C., Davini, S., et al. 2023, *A&A*, 670, A47, doi: [10.1051/0004-6361/202244445](https://doi.org/10.1051/0004-6361/202244445)
- Bos, E. G. P., van de Weygaert, R., Dolag, K., & Pettorino, V. 2012, *MNRAS*, 426, 440, doi: [10.1111/j.1365-2966.2012.21478.x](https://doi.org/10.1111/j.1365-2966.2012.21478.x)
- Bracewell, R. 1999, *The Fourier Transform and Its Applications*, 3rd ed. (McGraw-Hill), pp. 262–266
- Cai, Y.-C., Taylor, A., Peacock, J. A., & Padilla, N. 2016, *MNRAS*, 462, 2465, doi: [10.1093/mnras/stw1809](https://doi.org/10.1093/mnras/stw1809)
- Cautun, M., van de Weygaert, R., Jones, B. J. T., & Frenk, C. S. 2014, *MNRAS*, 441, 2923, doi: [10.1093/mnras/stu768](https://doi.org/10.1093/mnras/stu768)
- Chevallier, M., & Polarski, D. 2001, *International Journal of Modern Physics D*, 10, 213, doi: [10.1142/S0218271801000822](https://doi.org/10.1142/S0218271801000822)
- Chuang, C.-H., Yepes, G., Kitauro, F.-S., et al. 2019, *MNRAS*, 487, 48, doi: [10.1093/mnras/stz1233](https://doi.org/10.1093/mnras/stz1233)
- Contarini, S., Pisani, A., Hamaus, N., et al. 2023, *ApJ*, 953, 46, doi: [10.3847/1538-4357/acde54](https://doi.org/10.3847/1538-4357/acde54)
- . 2024, *A&A*, 682, A20, doi: [10.1051/0004-6361/202347572](https://doi.org/10.1051/0004-6361/202347572)
- Contarini, S., Ronconi, T., Marulli, F., et al. 2019, *MNRAS*, 488, 3526, doi: [10.1093/mnras/stz1989](https://doi.org/10.1093/mnras/stz1989)
- Contarini, S., Verza, G., Pisani, A., et al. 2022, *A&A*, 667, A162, doi: [10.1051/0004-6361/202244095](https://doi.org/10.1051/0004-6361/202244095)
- Correa, C. M., Paz, D. J., Padilla, N. D., et al. 2019, *MNRAS*, 485, 5761, doi: [10.1093/mnras/stz821](https://doi.org/10.1093/mnras/stz821)
- . 2022, *MNRAS*, 509, 1871, doi: [10.1093/mnras/stab3070](https://doi.org/10.1093/mnras/stab3070)
- Correa, C. M., Paz, D. J., Sánchez, A. G., et al. 2021, *MNRAS*, 500, 911, doi: [10.1093/mnras/staa3252](https://doi.org/10.1093/mnras/staa3252)
- Cousinou, M. C., Pisani, A., Tilquin, A., et al. 2019, *Astronomy and Computing*, 27, 53, doi: [10.1016/j.ascom.2019.03.001](https://doi.org/10.1016/j.ascom.2019.03.001)
- Degni et al. in prep
- DESI Collaboration, Adame, A. G., Aguilar, J., et al. 2024, arXiv e-prints, arXiv:2404.03002, doi: [10.48550/arXiv.2404.03002](https://doi.org/10.48550/arXiv.2404.03002)
- Dolag, K., Borgani, S., Murante, G., & Springel, V. 2009, *MNRAS*, 399, 497, doi: [10.1111/j.1365-2966.2009.15034.x](https://doi.org/10.1111/j.1365-2966.2009.15034.x)
- Eisenstein, D. J., Zehavi, I., Hogg, D. W., et al. 2005, *ApJ*, 633, 560, doi: [10.1086/466512](https://doi.org/10.1086/466512)
- Favole, G., Granett, B. R., Silva Lafaurie, J., & Sapone, D. 2021, *MNRAS*, 505, 5833, doi: [10.1093/mnras/stab1720](https://doi.org/10.1093/mnras/stab1720)
- Ferland, G. J., Porter, R. L., van Hoof, P. A. M., et al. 2013, *RMxAA*, 49, 137, doi: [10.48550/arXiv.1302.4485](https://doi.org/10.48550/arXiv.1302.4485)
- Foreman-Mackey, D., Farr, W., Sinha, M., et al. 2019, *The Journal of Open Source Software*, 4, 1864, doi: [10.21105/joss.01864](https://doi.org/10.21105/joss.01864)
- Fraser, T. S., Paillas, E., Percival, W. J., et al. 2024, arXiv e-prints, arXiv:2407.03221, doi: [10.48550/arXiv.2407.03221](https://doi.org/10.48550/arXiv.2407.03221)
- Goodman, J., & Weare, J. 2010, *Communications in Applied Mathematics and Computational Science*, 5, 65, doi: [10.2140/camcos.2010.5.65](https://doi.org/10.2140/camcos.2010.5.65)
- Hahn, O., Angulo, R. E., & Abel, T. 2015, *Monthly Notices of the Royal Astronomical Society*, 454, 3920
- Hamaus, N., Cousinou, M.-C., Pisani, A., et al. 2017, *JCAP*, 2017, 014, doi: [10.1088/1475-7516/2017/07/014](https://doi.org/10.1088/1475-7516/2017/07/014)
- Hamaus, N., Pisani, A., Choi, J.-A., et al. 2020, *JCAP*, 2020, 023, doi: [10.1088/1475-7516/2020/12/023](https://doi.org/10.1088/1475-7516/2020/12/023)
- Hamaus, N., Pisani, A., Sutter, P. M., et al. 2016, *PhRvL*, 117, 091302, doi: [10.1103/PhysRevLett.117.091302](https://doi.org/10.1103/PhysRevLett.117.091302)
- Hamaus, N., Sutter, P. M., & Wandelt, B. D. 2014, *PhRvL*, 112, 251302, doi: [10.1103/PhysRevLett.112.251302](https://doi.org/10.1103/PhysRevLett.112.251302)
- Hamaus, N., Aubert, M., Pisani, A., et al. 2022, *A&A*, 658, A20, doi: [10.1051/0004-6361/202142073](https://doi.org/10.1051/0004-6361/202142073)
- Hartlap, J., Simon, P., & Schneider, P. 2007, *A&A*, 464, 399, doi: [10.1051/0004-6361:20066170](https://doi.org/10.1051/0004-6361:20066170)
- Hawken, A. J., Aubert, M., Pisani, A., et al. 2020, *JCAP*, 2020, 012, doi: [10.1088/1475-7516/2020/06/012](https://doi.org/10.1088/1475-7516/2020/06/012)
- Hawken, A. J., Granett, B. R., Iovino, A., et al. 2017, *A&A*, 607, A54, doi: [10.1051/0004-6361/201629678](https://doi.org/10.1051/0004-6361/201629678)
- Jackson, J. C. 1972, *MNRAS*, 156, 1P, doi: [10.1093/mnras/156.1.1P](https://doi.org/10.1093/mnras/156.1.1P)
- Jennings, E., Li, Y., & Hu, W. 2013, *MNRAS*, 434, 2167, doi: [10.1093/mnras/stt1169](https://doi.org/10.1093/mnras/stt1169)
- Kaiser, N. 1987, *MNRAS*, 227, 1, doi: [10.1093/mnras/227.1.1](https://doi.org/10.1093/mnras/227.1.1)
- Kreisch, C. D., Pisani, A., Carbone, C., et al. 2019, *MNRAS*, 488, 4413, doi: [10.1093/mnras/stz1944](https://doi.org/10.1093/mnras/stz1944)
- Kreisch, C. D., Pisani, A., Villaescusa-Navarro, F., et al. 2022, *ApJ*, 935, 100, doi: [10.3847/1538-4357/ac7d4b](https://doi.org/10.3847/1538-4357/ac7d4b)
- Lahav, O., Lilje, P. B., Primack, J. R., & Rees, M. J. 1991, *MNRAS*, 251, 128, doi: [10.1093/mnras/251.1.128](https://doi.org/10.1093/mnras/251.1.128)
- Landy, S. D., & Szalay, A. S. 1993, *ApJ*, 412, 64, doi: [10.1086/172900](https://doi.org/10.1086/172900)
- Lavaux, G., & Wandelt, B. D. 2012, *ApJ*, 754, 109, doi: [10.1088/0004-637X/754/2/109](https://doi.org/10.1088/0004-637X/754/2/109)
- Lee, S. 2010, *Physics Letters B*, 685, 110, doi: [10.1016/j.physletb.2010.01.058](https://doi.org/10.1016/j.physletb.2010.01.058)
- Linder, E. V. 2003, *PhRvL*, 90, 091301, doi: [10.1103/PhysRevLett.90.091301](https://doi.org/10.1103/PhysRevLett.90.091301)

- . 2005, *PhRvD*, 72, 043529, doi: [10.1103/PhysRevD.72.043529](https://doi.org/10.1103/PhysRevD.72.043529)
- Mao, Q., Berlind, A. A., Scherrer, R. J., et al. 2017, *ApJ*, 835, 160, doi: [10.3847/1538-4357/835/2/160](https://doi.org/10.3847/1538-4357/835/2/160)
- Massara, E., Percival, W. J., Dalal, N., et al. 2022, *MNRAS*, 517, 4458, doi: [10.1093/mnras/stac2892](https://doi.org/10.1093/mnras/stac2892)
- Massara, E., Villaescusa-Navarro, F., Viel, M., & Sutter, P. M. 2015, *JCAP*, 2015, 018, doi: [10.1088/1475-7516/2015/11/018](https://doi.org/10.1088/1475-7516/2015/11/018)
- Merson, A., Wang, Y., Benson, A., et al. 2018, *MNRAS*, 474, 177, doi: [10.1093/mnras/stx2649](https://doi.org/10.1093/mnras/stx2649)
- N. H. Abel. 1842, *Oeuvres Completes*
- Nadathur, S., Percival, W. J., Beutler, F., & Winther, H. A. 2020a, *PhRvL*, 124, 221301, doi: [10.1103/PhysRevLett.124.221301](https://doi.org/10.1103/PhysRevLett.124.221301)
- Nadathur, S., Woodfinden, A., Percival, W. J., et al. 2020b, *MNRAS*, 499, 4140, doi: [10.1093/mnras/staa3074](https://doi.org/10.1093/mnras/staa3074)
- Neyrinck, M. C. 2008, *MNRAS*, 386, 2101, doi: [10.1111/j.1365-2966.2008.13180.x](https://doi.org/10.1111/j.1365-2966.2008.13180.x)
- Pace, F., Waizmann, J. C., & Bartelmann, M. 2010, *MNRAS*, 406, 1865, doi: [10.1111/j.1365-2966.2010.16841.x](https://doi.org/10.1111/j.1365-2966.2010.16841.x)
- Paz, D., Lares, M., Ceccarelli, L., Padilla, N., & Lambas, D. G. 2013, *MNRAS*, 436, 3480, doi: [10.1093/mnras/stt1836](https://doi.org/10.1093/mnras/stt1836)
- Peacock, J. A., & Heavens, A. F. 1990, *MNRAS*, 243, 133, doi: [10.1093/mnras/243.1.133](https://doi.org/10.1093/mnras/243.1.133)
- Peebles, P. J. E. 1980, *The large-scale structure of the universe*
- Pellicciari, D., Contarini, S., Marulli, F., et al. 2023, *MNRAS*, 522, 152, doi: [10.1093/mnras/stad956](https://doi.org/10.1093/mnras/stad956)
- Pisani, A., Lavaux, G., Sutter, P. M., & Wandelt, B. D. 2014, *MNRAS*, 443, 3238, doi: [10.1093/mnras/stu1399](https://doi.org/10.1093/mnras/stu1399)
- Pisani, A., Sutter, P. M., Hamaus, N., et al. 2015a, *PhRvD*, 92, 083531, doi: [10.1103/PhysRevD.92.083531](https://doi.org/10.1103/PhysRevD.92.083531)
- Pisani, A., Sutter, P. M., & Wandelt, B. D. 2015b, *arXiv e-prints*, arXiv:1506.07982, doi: [10.48550/arXiv.1506.07982](https://doi.org/10.48550/arXiv.1506.07982)
- Planck Collaboration, Ade, P. A. R., Aghanim, N., et al. 2016, *A&A*, 594, A13, doi: [10.1051/0004-6361/201525830](https://doi.org/10.1051/0004-6361/201525830)
- Platen, E., van de Weygaert, R., & Jones, B. J. T. 2007, *MNRAS*, 380, 551, doi: [10.1111/j.1365-2966.2007.12125.x](https://doi.org/10.1111/j.1365-2966.2007.12125.x)
- Pollina, G., Hamaus, N., Dolag, K., et al. 2017, *MNRAS*, 469, 787, doi: [10.1093/mnras/stx785](https://doi.org/10.1093/mnras/stx785)
- Radinović, S., Winther, H. A., Nadathur, S., et al. 2024, *arXiv e-prints*, arXiv:2407.02699, <https://arxiv.org/abs/2407.02699>
- Radinović, S., Nadathur, S., Winther, H. A., et al. 2023, *A&A*, 677, A78, doi: [10.1051/0004-6361/202346121](https://doi.org/10.1051/0004-6361/202346121)
- Raveri, M., Doux, C., & Pandey, S. 2024, *arXiv e-prints*, arXiv:2409.09101, doi: [10.48550/arXiv.2409.09101](https://doi.org/10.48550/arXiv.2409.09101)
- Ryden, B. S. 1995, *ApJ*, 452, 25, doi: [10.1086/176277](https://doi.org/10.1086/176277)
- Sahlén, M. 2019, *PhRvD*, 99, 063525, doi: [10.1103/PhysRevD.99.063525](https://doi.org/10.1103/PhysRevD.99.063525)
- Sahlén, M., Zubeldía, Í., & Silk, J. 2016, *ApJL*, 820, L7, doi: [10.3847/2041-8205/820/1/L7](https://doi.org/10.3847/2041-8205/820/1/L7)
- Sánchez, A. G. 2020, *PhRvD*, 102, 123511, doi: [10.1103/PhysRevD.102.123511](https://doi.org/10.1103/PhysRevD.102.123511)
- Schaap, W. E., & van de Weygaert, R. 2000, *A&A*, 363, L29, <https://arxiv.org/abs/astro-ph/0011007>
- Schuster, N., Hamaus, N., Dolag, K., & Weller, J. 2023, *JCAP*, 2023, 031, doi: [10.1088/1475-7516/2023/05/031](https://doi.org/10.1088/1475-7516/2023/05/031)
- . 2024, *JCAP*, 2024, 065, doi: [10.1088/1475-7516/2024/08/065](https://doi.org/10.1088/1475-7516/2024/08/065)
- Schuster, N., Hamaus, N., Pisani, A., et al. 2019, *JCAP*, 2019, 055, doi: [10.1088/1475-7516/2019/12/055](https://doi.org/10.1088/1475-7516/2019/12/055)
- Shandarin, S. F. 2011, *JCAP*, 2011, 015, doi: [10.1088/1475-7516/2011/05/015](https://doi.org/10.1088/1475-7516/2011/05/015)
- Sheth, R. K., Mo, H. J., & Tormen, G. 2001, *MNRAS*, 323, 1, doi: [10.1046/j.1365-8711.2001.04006.x](https://doi.org/10.1046/j.1365-8711.2001.04006.x)
- Sheth, R. K., & van de Weygaert, R. 2004, *MNRAS*, 350, 517, doi: [10.1111/j.1365-2966.2004.07661.x](https://doi.org/10.1111/j.1365-2966.2004.07661.x)
- Spergel, D., Gehrels, N., Baltay, C., et al. 2015, *arXiv e-prints*, arXiv:1503.03757, doi: [10.48550/arXiv.1503.03757](https://doi.org/10.48550/arXiv.1503.03757)
- Springel, V., Yoshida, N., & White, S. D. M. 2001, *NewA*, 6, 79, doi: [10.1016/S1384-1076\(01\)00042-2](https://doi.org/10.1016/S1384-1076(01)00042-2)
- Sutter, P. M., Lavaux, G., Hamaus, N., et al. 2014a, *MNRAS*, 442, 462, doi: [10.1093/mnras/stu893](https://doi.org/10.1093/mnras/stu893)
- . 2014b, *MNRAS*, 442, 462, doi: [10.1093/mnras/stu893](https://doi.org/10.1093/mnras/stu893)
- . 2015, *Astronomy and Computing*, 9, 1, doi: [10.1016/j.ascom.2014.10.002](https://doi.org/10.1016/j.ascom.2014.10.002)
- Thiele, L., Massara, E., Pisani, A., et al. 2024, *ApJ*, 969, 89, doi: [10.3847/1538-4357/ad434e](https://doi.org/10.3847/1538-4357/ad434e)
- Verza, G., Carbone, C., Pisani, A., Porciani, C., & Matarrese, S. 2024, *JCAP*, 2024, 079, doi: [10.1088/1475-7516/2024/10/079](https://doi.org/10.1088/1475-7516/2024/10/079)
- Verza, G., Carbone, C., Pisani, A., & Renzi, A. 2023, *JCAP*, 2023, 044, doi: [10.1088/1475-7516/2023/12/044](https://doi.org/10.1088/1475-7516/2023/12/044)
- Verza, G., Carbone, C., & Renzi, A. 2022, *ApJL*, 940, L16, doi: [10.3847/2041-8213/ac9d98](https://doi.org/10.3847/2041-8213/ac9d98)
- Verza, G., Pisani, A., Carbone, C., Hamaus, N., & Guzzo, L. 2019, *JCAP*, 2019, 040, doi: [10.1088/1475-7516/2019/12/040](https://doi.org/10.1088/1475-7516/2019/12/040)
- Wang, Y., Zhai, Z., Alavi, A., et al. 2022, *The Astrophysical Journal*, 928, 1, doi: [10.3847/1538-4357/ac4973](https://doi.org/10.3847/1538-4357/ac4973)
- Woodfinden, A., Nadathur, S., Percival, W. J., et al. 2022, *MNRAS*, 516, 4307, doi: [10.1093/mnras/stac2475](https://doi.org/10.1093/mnras/stac2475)

Woodfinden, A., Percival, W. J., Nadathur, S., et al. 2023,
MNRAS, 523, 6360, doi: [10.1093/mnras/stad1725](https://doi.org/10.1093/mnras/stad1725)

Xu, X., Cuesta, A. J., Padmanabhan, N., Eisenstein, D. J.,
& McBride, C. K. 2013, MNRAS, 431, 2834,
doi: [10.1093/mnras/stt379](https://doi.org/10.1093/mnras/stt379)
Zel'dovich, Y. B. 1970, A&A, 5, 84
Zhai, Z., Chuang, C.-H., Wang, Y., Benson, A., & Yepes, G.
2021, MNRAS, 501, 3490, doi: [10.1093/mnras/staa3911](https://doi.org/10.1093/mnras/staa3911)